MECHANICAL ENGINEERING SCIENCE

ISSN:2661-4448(online)
2661-443X(print)
Volume 4 No.1 2022

VISER
www.viserdata.com

COMPANY INTRODUCTION

Viser Technology Pte. Ltd. was founded in Singapore with branch offices in both Hebei and Chongqing, China. Viser focuses on publishing scientific and technological journals and books that promote the exchange of scientific and technological findings among the research community and around the globe. Despite being a young company, Viser is actively connecting with well-known universities, research institutes, and indexation database, and has already established a stable collaborative relationship with them. We also have a group of experienced editors and publishing experts who are dedicated to publishing high-quality journal and book contents. We offer the scholars various academic journals covering a variety of subjects and we are committed to reducing the hassles of scholarly publishing. To achieve this goal, we provide scholars with an all-in-one platform that offers solutions to every publishing process that a scholar needs to go through in order to show their latest finding to the world.

Mechanical Engineering Science

Honorary Editor-in-Chief: Kuangchao Fan

Editor-in-Chief: Zhaoyao SHI

Associate Editors: Jinliang XU Yan SHI Jianlian CHENG

Editorial Board Members:

Haihui CHEN	Ailun WANG	Chun CHEN	Chunlei YANG	Yuliang ZHANG
Yajun HUI	Jigang WU	Liangbo SUN	Fanglong YIN	Wei LIANG
Weixia DONG	Hongbo LAN	Wenjun MENG	Xi ZHANG	Wanqing SONG
Shilong QI	Yiqi WANG	Qiang JIANG	Yunjun LIU	Fei GAO
Yongfeng SHEN	Daoguang HE	Yi QIN	Xiaolan SONG	Jianbo YU
Hui SUN	Qingyang WANG	Guodong SUN	Xiaolong WANG	Yong ZHU
Jianzhuo ZHANG	Qingshuang Chen	Jianxiong YE	Kun XIE	Shaohua LUO
Mingsong CHEN	Jun TIAN	Qinjian ZHANG	Jingying SUN	Jiangmiao YU
Dabin CUI	Jing WEI	Daoyun CHEN	Jianhui LIN	Zhinan YANG
Wenfeng LIANG	Hongbo YAN	Yefa HU	Cai YI	Suyun TIAN
Hua ZHANG	Lingyun YAO	Xiangjie YANG	Zhijian WANG	Ying LI
Jianmei WANG	Peiqi LIU	Chunsheng SONG	Yeming ZHANG	Kongyin ZHAO
Xiaowei ZHANG	Wei LIU	Honglin GAO	Zhichao LOU	Yanfeng GAO

Publisher: Viser Technology Pte. Ltd.

ISSN: 2661-4448(online)

2661-443X(print)

Frequency: Semi-annual

Add.:21 Woodlands Close, #08-18

Primz Bizhub SINGAPORE (737854)

https://www.viserdata.com/

Editors:

Yajun LIAN Yanli LIU

John WILSON Nike Yough

Mart CHEN Qiuyue SU

Debra HAMILTON Xin DI

Jennifer M DOHY Xiuli LI

Edward Adam Davis

Designer: Anson CHEE

Copyright © 2022 by authors and Viser Technology Pte. Ltd.

Mechanical Engineering Science

Volume 4 No.1 (2022)

CONTENTS

VISER

Viser Technology Pte. Ltd.
Mechanical Engineering Science
DOI: 10.33142/mes.v4i1.7511

Research Article Open Access

Uncertainty-based Multidisciplinary Design Optimization using An Approximated Second-Order Reliability Analysis Strategy

Zhiyuan LYU[1], Hongtao WANG[1], Hengfei YANG[1], Jiapeng WANG[1], Ketema Mikiyas Solomon[1], Debiao MENG[1,2,3*]

1. School of Mechanical and Electrical Engineering, University of Electronic Science and Technology of China, Chengdu 611731, China
2. Institute of Electronic and Information Engineering of UESTC in Guangdong, Dongguan 523808, China
3. Yangzhou Yangjie Electronic Technology Co., Ltd., Jiangsu Yangzhou 225008, China

***Corresponding Author:** Debiao Meng, E-mail address: dbmeng@uestc.edu.cn*

Abstract:
In uncertainty-based multidisciplinary design optimization (UBMDO), all reliability limitation factors are maintained due to minimize the cost target function. There are many reliability evaluation methods for reliability limitation factors. The second-order reliability method (SORM) is a powerful most possible point (MPP)-based method. It can provide an accurate estimation of the failure probability of a highly nonlinear limit state function despite its large curvature. But the Hessian calculation is necessary in SORM, which results in a heavy computational cost. Recently, an efficient approximated second-order reliability method (ASORM) is proposed. The ASORM uses a quasi-Newton method to close to Hessian without the direct calculation of Hessian. To further improve the UBMDO efficiency, we also introduce the performance measure approach (PMA) and the sequential optimization and reliability assessment (SORA) strategy. To solve the optimization design problem of a turbine blade, the formula of MDO with ASORM under the SORA framework (MDO-ASORM-SORA) is proposed.

Keywords: *uncertainty; reliability analysis; optimization design; turbine blade*

Introduction

The Multidisciplinary design optimization (MDO) is a methodology for the design problems of complicated and coupled engineering systems, which has received extensive attention from industry and academia [1-11]. The application of MDO research results has expanded from the initial hypersonic aircraft, large passenger aircraft, shuttle spacecraft, and other aerospace fields to vehicles and ships, electronics, energy, and civil and construction and other engineering fields have produced significant technical and economic benefits [12-16]. To effectively consider the influence of these uncertain factors in the process of design optimization, uncertainty-based multidisciplinary design optimization (UBMDO) has become one of the research hot spots of modern engineering system design [17-26]. So far, the UBMDO method that considers random uncertainty has become more mature after combining reliability analysis methods such as classical probability theory. Due to the adoption of the sequence optimization and reliability evaluation sequential optimization and reliability assessment (SORA) strategy, the reliability analysis process and the design optimization process are decoupled [27-29]. The entire

UBMDO process is decomposed into a series of alternate deterministic MDO and reliability analysis processes, and the computational efficiency is further improved [30-31].

However, the Hessian calculation is necessary in second-order reliability method (SORM), which results in a heavy computational cost. To further improve the efficiency and robustness of UBMDO, based on UBMDO, the approximated second-order reliability method (ASORM) method based on performance measure approach (PMA) under SORA strategy is proposed.

1 Traditional reliability calculation method

1.1 First order reliability method (FORM)

For the limit state equation $G(x)=0$, x is

Copyright © 2022 by author(s) and Viser Technology Pte. Ltd. This is an Open Access article distributed under the terms of the Creative Commons Attribution-NonCommercial 4.0 International License (http://creativecommons.org/licenses/by-nc/4.0/), permitting all non-commercial use, distribution, and reproduction in any medium, provided the original work is properly cited.
Received on February 11, 2022; Accepted on May 20, 2022

represented as a vector form of a random variable in the original space, which is transformed into an independent standard normal space (U space), and the limit state equation will be rewritten as $g(u)=0$. According to the physical meaning of the reliability index, the problem of calculating the reliability index is transformed into the problem of solving the minimum distance from the origin of the coordinate to the limit state surface in U space. The specific constrained optimization problem is as follows:

When $g(u)=0$, compute the $u^*=\min_n\|u\|$, So the first-order reliability index β^{FORM} and the instability probability $P_{\mathrm{f}}^{\mathrm{FORM}}$ are computed by Eq. (1):

$$\begin{aligned}\beta^{\mathrm{FORM}}&=\|u^*\|\\ P_{\mathrm{f}}^{\mathrm{FORM}}&\approx\Phi\left(-\beta^{\mathrm{FORM}}\right)\end{aligned}\tag{1}$$

where $\|\bullet\|$ is the modulus of the vector, Φ is the standard normal distribution function.

1.2 The review of SORM

The SORM method uses Taylor series to expand the function $g(u)$ at point u^*, and keeps the quadratic term. The second-order approximate expression of $g(u)$ can be obtained as follow:

$$g(u)=\beta^{\mathrm{FORM}}-\alpha^T u+\frac{1}{2}\left(u-u^*\right)^T H\left(u-u^*\right)\tag{2}$$

where $\alpha=-\dfrac{\nabla g\left(u^*\right)}{\left|\nabla g\left(u^*\right)\right|}$ is the unit direction vector at the verification point in U space, $H=\dfrac{\nabla^2 g\left(u^*\right)}{\left|\nabla g\left(u^*\right)\right|}$ is the n-dimensional Hessian matrix, n is the number of random variables, $\nabla g(u)$ is the gradient vector of the verification point u^*, which can use the front difference method to calculate:

$$\nabla g(u)_i=\frac{g\left(u_i+\Delta h\right)-g\left(u_i\right)}{\Delta h}\tag{3}$$

where Δh is the step size, i is the ith component of the vector.

On the basis of the obtained verification point u^* and the Hessian matrix H, the random variable is transferred from U space to V space to ensure that the nth axis of V space coincides with the verification point vector u^*, which can be solved by the Gram-Schmidt method. The matrix form is V=PU. Operate the rotation matrices P and H, select the first n-1 order to form a sub-matrix, and perform diagonal processing on the sub-matrix to obtain the n-1 order diagonal matrix H_{rot} as follows:

$$H_{rot}=P\frac{H}{\left\|\nabla g\left(u^*\right)\right\|}P^T\tag{4}$$

The diagonal element of the matrix H_{rot} is the principal curvature κ_i, which is $\kappa_i=\left[H_{rot}\right]_{ii}(i=1,2,\mathrm{L}\ ,n-1)$. Geometrically, κ_i represents the principal curvature at the check point. After obtaining the check point and principal curvature, different algorithms can be used to calculate the second-order reliability.

2 The approximated second-order reliability method

In UBMDO, the evaluation of the reliability constraints can be defined using a multidimensional integral. However, when the limit state functions are nonlinear, the multidimensional integral cannot be calculated analytically. Therefore, we approximate the limit state function by the Taylor series of second-order at the MPP in U-space.

To eliminate the mistake caused by quadratic function parabolic approximation and obtain a better accuracy, this study uses the SORM with the generalized chi-square distribution.

In practical engineering problems, the calculation of Hessian analysis cannot be performed. To solve previous problem, utilizing the quasi-Newton approach to approximate the Hessian. This paper also introduces the ASORM.

When being close to the N×N Hessian matrix, taking a symmetric matrix, there are N(N+1)/2 degrees of freedom, while the secant line term exerts only N constraints. the unique Hessian updates required additional constraints. The symmetric rank-one (SR1) updates and creates the unique symmetric matrix with a rank-one amendment meeting the secant qualification.

Finding a FORM calculation method with good convergence is the basis for calculating SORM indicators. In this paper, the HLRF-BFGS algorithm [32] is used to determine the check point to obtain the first-order reliability index; then the SR1 algorithm is used to approximate the Hessian matrix to obtain the second-order reliability index with excellent accuracy.

Based on the FORM calculation process of the HLRF-BFGS algorithm, the search calculation direction d_k can be obtained by the Eq. (5):

$$\begin{aligned}d_k=&\frac{\left[\nabla g\left(u_{k-1}\right)^T B_{k-1}^{\mathrm{BFGS}}u_{k-1}-g\left(u_{k-1}\right)\right]}{\nabla g\left(u_{k-1}\right)^T B_{k-1}^{\mathrm{BFGS}}\nabla g\left(u_{k-1}\right)}\\ &B_{k-1}^{\mathrm{BFGS}}\nabla g\left(u_{k-1}\right)-B_{k-1}^{\mathrm{BFGS}}u_{k-1}\end{aligned}\tag{5}$$

$$B_k^{\mathrm{BFGS}} = B_{k-1}^{\mathrm{BFGS}} + \left(1 + \frac{q_k^T B_{k-1}^{\mathrm{BFGS}} q_k}{d_k^T q_k}\right)\frac{d_k d_k^T}{d_k^T q_k} - \frac{d_k q_k^T B_{k-1}^{\mathrm{BFGS}} + B_{k-1}^{\mathrm{BFGS}} q_k d_k^T}{d_k^T q_k} \tag{6}$$

where k is the number of iterations; B^{BFGS} is the inverse matrix of the Hessian matrix calculated by the BFGS algorithm, that is $B^{\mathrm{BFGS}} = \left(H^{\mathrm{BFGS}}\right)^{-1}$, which can be obtained by the recursive Eq. (6). q_k is expressed as Eq. (7):

$$q_k = d_k + \left[\nabla g\left(u_k\right) - \nabla g\left(u_{k-1}\right)\right]\xi_k \tag{7}$$

where $\xi_k = \dfrac{g\left(u_{k-1}\right) - \nabla g\left(u_{k-1}\right)^T B_{k-1}^{\mathrm{BFGS}} u_{k-1}}{\nabla g\left(u_{k-1}\right)^T B_{k-1}^{\mathrm{BFGS}} \nabla g\left(u_{k-1}\right)}$.

On this basis, the check point in the new iteration can be obtained by the Eq. (8):

$$u_k = u_{k-1} + d_k \tag{8}$$

Repeat the above iteration process, the iteration stops when the following conditions are met: $1 - \dfrac{\left|\nabla g\left(u_k\right)^T u_k\right|}{\left\|\nabla g\left(u_k\right)\right\| \cdot \left\|u_k\right\|} < \varepsilon$ and $\left|g\left(u_k\right)\right| < \varepsilon$.

At the same time, the SR1 algorithm can provide a more accurate approximation of the Hessian matrix than other methods. Therefore, SR1 algorithm is used to approximate the Hessian matrix in each iteration in this study. Its expression is as follow:

$$H_k^{\mathrm{SR1}} = H_{k-1}^{\mathrm{SR1}} + \frac{\left(y_k - H_{k-1}^{\mathrm{SR1}} d_k\right)\left(y_k - H_{k-1}^{\mathrm{SR1}} d_k\right)^T}{\left(y_k - H_{k-1}^{\mathrm{SR1}} d_k\right)^T d_k} \tag{9}$$

where $y_k = \nabla g\left(u_k\right) - \nabla g\left(u_{k-1}\right)$.

Compared with SORM, ASORM adopts the approximated Hessian rather than direct calculation of Hessian. Thereby it requires computations only used in FORM to realize much efficient and precise reliability analysis. Compared with FORM, in the most possible point (MPP) search, ASORM makes full use of the information collected, Thus the reliability assessment can be more accurate.

3 Review of PMA and SORA

3.1 The PMA

In UBMDO, adopting PMA is more effective than direct evaluation of actual probability. If some non-active reliability restrictions are directly evaluated to get their real probabilities, they will govern the entire calculation process, leading to low computational efficiency.

The basic formula of UBMDO is to minimize the objective function under the restriction of probability, which can be expressed as Eq. (10).

$$\begin{aligned} &\min_{(d_s, d_i, x_s, x_i)} \ f\left(d_s, d_i, x_s, x_i\right), \\ &s.t. \quad J_1\left(d_s, d_i, x_s, x_i\right) \le \varepsilon, \\ &\quad J_2\left(d_s, d_i, x_s, x_i\right) \le \varepsilon, \\ &\quad \Pr\left\{g_i\left(d_s, d_i, x_s, x_i\right) \le 0\right\} \ge R \\ &\quad d_s^L \le d_s \le d_s^U, \\ &\quad d_i^L \le d_i \le d_i^U, \\ &\quad x_s^L \le x_s \le x_s^U, \\ &\quad x_i^L \le x_i \le x_i^U \\ &\quad i = 1, 2 \end{aligned} \tag{10}$$

where the $f(\bullet)$ indicates the objective function of UBMDO problem. di represents the local design variables for the i th discipline. ds are shared design variables in all disciplines. xi express the local input variables for discipline i, xs denotes the vector of sharing variables which are input variables of every discipline. $\Pr\left(g^{(i)} > 0\right) \le \alpha_t$ are probability restrictions to discipline i. $\Pr\left(g > 0\right)$ refers to the probability of fail with the pattern of $g > 0$. J1 and J2 are the flabby limitation requirements of subsystem 1 and subsystem 2, severally. ε represents an extremely small positive number that can be dynamically changeable. gi and Ri signify the probability limitation requirements and allowed reliability separately.

To every probability restriction, the PMA-based UBMDO can be depicted as Eq. (11).

$$\begin{aligned} &\min_{\left(u_s^{(i)}, u_i^{(i)}\right)} \ g^{(i)}\left(d_s, d_i, u_s^{(i)}, u_i^{(i)}\right) \\ &s.t. \ \left\|\left(u_s^{(i)}, u^{(i)}\right)\right\| = \beta_t \\ &i = 1, 2, \mathrm{L}\ , n \end{aligned} \tag{11}$$

where $u_s^{(i)}$ and $u_i^{(i)}$ are the standard normal stochastic variables for U-space, they separately denote stochastic variables of x_s and x_i of discipline i in X-space. β_t is the required reliability. $u^{(i)}$ consists of all standard normal stochastic variables in all disciplines.

3.2 The SORA strategy

In UBMDO, The SORA adopts series of cycles for reliability analysis and decoupled deterministic MDO. In every cycle, reliability analysis and MDO are mutually decoupled. Reliability analysis is performed after MDO, and the process of SORA is demonstrated. The ASORM is used to work out the reliability estimation problems in a cycle in this study. Use PMA to construct a new deterministic MDO problem for the next cycle within the framework of SORA.

4 The turbine blade design optimization

In this paper, the UBMDO which only considers interval variables is improved, and both interval variables and random variables are considered in the

optimization design process. Then, taking the optimal design of the planetary gearbox for a megawatt wind turbine as the research object, the uncertainty factors in the optimal design of the wind turbine planetary gearbox are analyzed. On this basis, the proposed method is used to optimize the design of the planetary gearbox. The final comparative analysis shows the result of planetary gearbox optimization, and the optimization design scheme of this paper is feasible.

Turbine blades are important components which make up the turbine section of a gas turbine [33-34]. The blades extract energy from the high temperature, high pressure gas produced by the combustor, thus the turbine blade design optimization is a typical MDO problem including heat transfer, aerodynamics and structure. In this study, a turbine blade design optimization problem is solved using the proposed UBMDO method. The objective is maximizing the aerodynamic efficiency η. There are nine design variables and three constraints, which are shown in Figure 1 and Tab. 1.

Here, we assume that all design variables are random variables which are normally distributed. We use FORM, SORM and ASORM to solve this MDO problem, respectively. In Tab. 2, we can see that all reliability estimation methods can obtain reasonable solutions. The UBMDO methods using ASORM and using FORM require almost the same computation time t. However, the aerodynamic efficiency from UBMDO using ASORM are more conservative than that from UBMDO using FORM. Compared with the aerodynamic efficiency η=0.9428 from UBMDO using SORM, the aerodynamic efficiency from UBMDO using ASORM is 0.9468. It means that two UBMDO methods can enjoy higher accurate reliability estimations.

Table 1 Design variables and constraints of turbine blade design optimization

			Description	Initial value	Lower bound	Upper bound
Design variables	Top section	r_1 / r_2 / r_3	Installation angle	41.0/61.0/74.0	38.0/58.0/71.0	44.0/64.0/77.0
	Middle section	φ_1 / φ_2 / φ_3	Incidence angle	10.0/2.0/-6.0	7.0/0.5/-9.0	13.0/5.0/-3.0
	Root section	ξ_1 / ξ_2 / ξ_3	Deviation angle	6.0/4.0/2.0	3.0/1.0/0.5	9.0/7.0/5.0
Constraints	Maximum temperature/K			983.22	-	1000
	Equivalent stress/MPa			603.09	-	120
	Maximum deformation/mm			0.5012	-	0.6

Table 2 Design variables and constraints of turbine blade design optimization

	r_1	φ_1	ξ_1	r_2	φ_2	ξ_2	r_3	φ_3	ξ_3	η	t
ASORM	38.17	11.09	6.56	57.08	4.66	6.15	71.97	-4.97	1.06	0.9468	72hr/43min
SORM	38.42	11.23	6.37	56.35	4.71	6.44	71.35	-4.58	1.10	0.9428	129hr/39min
FORM	36.34	10.34	6.53	55.30	4.89	6.92	73.01	-4.55	1.28	0.9613	69hr/39min

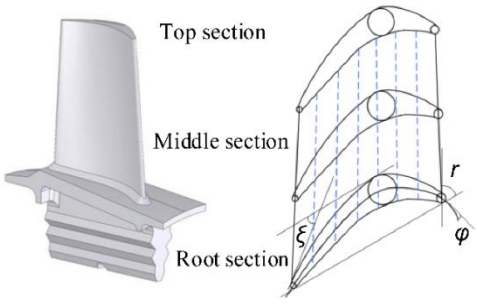

Figure 1 The structure sketch of a turbine blade

5 Conclusion

In UBMDO, the computational cost of the objective function is minimized while preserving all reliability constraints. There are many methods of reliability assessment. SORM is an MPP-based method. It can accurately estimate the failure probability of highly nonlinear limit state functions. However, Hessian calculation is required in SORM, and the calculation cost is very high. Recently, an efficient ASORM has been proposed. ASORM uses the quasi-Newton method to approximate the Hessian without directly computing the Hessian. To further improve UBMDO efficiency, we also introduce PMA and SORA strategies. To solve the optimal design problem of turbine blades, MDO-ASORM-SORA is proposed. It is demonstrated that the proposed method has more accurate reliability estimates.

Acknowledgments

This research was funded by the National Natural Science Foundation of China (Grant No. 52175130), the Sichuan Science and Technology Program (Grant No. 2022YFQ0087), the China Postdoctoral Science Foundation (Grant No. 2021M700693), the Guangdong Basic and Applied Basic Research Foundation (Grant No. 2021A1515012070), and the Sichuan Science and Technology Innovation Seedling Project Funding Project (Grant No. 2021112).

References

[1] Meng D, Xie T, Wu P, et al., 2020. Uncertainty-based design and optimization using first order saddle point approximation method for multidisciplinary engineering systems. ASCE-ASME Journal of Risk and Uncertainty in Engineering Systems, Part A: Civil Engineering, 6(3): 04020028.

[2] Wang Y H, Zhang, C Su, et al., 2019. Structure optimization of the frame based on response surface method. International Journal of Structural Integrity, 11(3):411-425.

[3] Li L, Wan H, Gao W, et al., 2019. Reliability based multidisciplinary design optimization of cooling turbine blade considering uncertainty data statistics. Structural and multidisciplinary optimization, 59(2):659-673.

[4] Wang L, Xiong C, Yang Y, 2018. A novel methodology of reliability-based multidisciplinary design optimization under hybrid interval and fuzzy uncertainties. Computer Methods in Applied Mechanics and Engineering, 337: 439-457.

[5] Wang X, Wang R, Wang L, et al., 2018. An efficient single-loop strategy for reliability-based multidisciplinary design optimization under non-probabilistic set theory. Aerospace Science and Technology, 73:148-163.

[6] Li X Q, Song L K, Bai G C, 2021. Recent advances in reliability analysis of aeroengine rotor system: a review. International Journal of Structural Integrity, 13(1): 1-29.

[7] Li Y H, Sheng Z, Zhi P, et al., 2019. Multi-objective optimization design of anti-rolling torsion bar based on modified NSGA-III algorithm. International Journal of Structural Integrity, 12(1):17-30.

[8] Periçaro G A, Santos S R, Ribeiro A A, et al., 2015. HLRF–BFGS optimization algorithm for structural reliability. Applied Mathematical Modelling, 39(7):2025-2035.

[9] Tian W, Heo Y, De Wilde P, et al., 2018. A review of uncertainty analysis in building energy assessment. Renewable and Sustainable Energy Reviews, 93:285-301.

[10] Li Y H, Zhang C, Yin H, et al., 2021. Modification optimization-based fatigue life analysis and improvement of EMU gear. International Journal of Structural Integrity, 12(5):760-772.

[11] Li X Q, Song L K, Bai G C, 2021. Recent advances in reliability analysis of aeroengine rotor system: a review. International Journal of Structural Integrity, 13(1):1-29.

[12] Wang Z, Huang W, Yan L, 2014. Multidisciplinary design optimization approach and its application to aerospace engineering. Chinese science bulletin, 59(36):5338-5353.

[13] Miao B R, Luo Y X, Peng Q M, et al., 2020. Multidisciplinary design optimization of lightweight carbody for fatigue assessment. Materials & design, 194:108910.

[14] Li W, Gao L, Garg A, et al., 2020. Multidisciplinary robust design optimization considering parameter and metamodeling uncertainties. Engineering with Computers:1-18.

[15] Peixun Y U, Jiahui P, Junqiang B, et al., 2020. Aeroacoustic and aerodynamic optimization of propeller blades. Chinese Journal of Aeronautics, 33(3):826-839.

[16] Han A, Wohn K, Ahn J, 2021. Towards new fashion design education: learning virtual prototyping using E-textiles. International Journal of Technology and Design Education, 31(2):379-400.

[17] Li L, Wan H, Gao W, et al., 2019. Reliability based multidisciplinary design optimization of cooling turbine blade considering uncertainty data statistics. Structural and multidisciplinary optimization, 59(2):659-673.

[18] Keshtegar B, Hao P, 2018. Enriched self-adjusted performance measure approach for reliability-based design optimization of complex engineering problems. Applied Mathematical Modelling, 57:37-51.

[19] Keshtegar B, Meng, D, Ben Seghier, et al., 2021. A hybrid sufficient performance measure approach to improve robustness and efficiency of reliability-based design optimization. Engineering with Computers, 37(3):1695-1708.

[20] Meng D, Li Y F, Huang H Z, et al., 2015. Reliability-based multidisciplinary design optimization using subset simulation analysis and its application in the hydraulic transmission mechanism design. Journal of Mechanical Design, 137(5): 051402.

[21] Meng D, Yang S, Lin T, et al., 2022. RBMDO using gaussian mixture model-based second-order mean-value saddlepoint approximation. CMES-Computer Modeling in Engineering & Sciences, 132(2): 553-568.

[22] Ahn J, Kwon J H, 2006. An efficient strategy for reliability-based multidisciplinary design optimization using BLISS. Structural and Multidisciplinary Optimization, 31(5):363-372.

[23]Jung Y, Cho H, Lee I, 2019. Reliability measure approach for confidence-based design optimization under insufficient input data. Structural and Multidisciplinary Optimization, 60(5):1967-1982.

[24] Zhang X, Huang H Z, Zeng S, et al., 2009. Possibility-based multidisciplinary design optimization in the framework of sequential optimization and reliability assessment. In International Design Engineering Technical Conferences and Computers and Information in Engineering Conference, 49002:745-750.

[25] Meng D, Yang S, de Jesus A M, Zhu S P, 2022. A novel Kriging-model-assisted reliability-based multidisciplinary design optimization strategy and its application in the offshore wind turbine tower. Renewable Energy. https://doi.org/10.1016/j.renene.2022.12.62.

[26] Clark C E, DuPont B, 2018. Reliability-based design optimization in offshore renewable energy systems. Renewable and Sustainable Energy Reviews, 97:390-400.

[27] Du X, Guo J, Beeram, H, 2008. Sequential optimization and reliability assessment for multidisciplinary systems design. Structural and Multidisciplinary Optimization, 35(2):117-130.

[28] Meng D, Yang S, Zhang Y, et al., 2019. Structural reliability analysis and uncertainties-based collaborative design and optimization of turbine blades using surrogate model. Fatigue & Fracture of Engineering Materials & Structures, 42(6):1219-1227.

[29] Meng D, Yang S, He C, et al., 2022. Multidisciplinary design optimization of engineering systems under uncertainty: a review. International Journal of Structural Integrity, 13(4), 565-593.

[30] Meng D, Lv Z, Yang S, et al., 2021. A time-varying mechanical structure reliability analysis method based on performance degradation. In Structures, 34:3247-3256.

[31] Luo C, Keshtegar B, Zhu S P, et al., 2022. Hybrid enhanced Monte Carlo simulation coupled with advanced machine learning approach for accurate and efficient structural reliability analysis. Computer Methods in Applied Mechanics and Engineering, 388:114218.

[32] Periçaro G A, Santos S R, Ribeiro A A, et al., 2015. HLRF–BFGS optimization algorithm for structural reliability. Applied Mathematical Modelling, 39(7):2025-2035.

[33] Meng D, Wang H, Yang S, et al., 2022. Fault analysis of wind power rolling bearing based on EMD feature extraction. CMES-Computer Modeling in Engineering & Sciences, 130(1), 543-558.

[34] Yang S, Wang J, Yang H, 2022. Evidence theory based uncertainty design optimization for planetary gearbox in wind turbine. Journal of Advances in Applied & Computational Mathematics, 9: 86-102.

Viser Technology Pte. Ltd.
Mechanical Engineering Science
DOI: 10.33142/mes.v4i1.7512

Research Article Open Access

Reliability analysis of small failure probability based on subset simulation method

Hongtao WANG*, Ketema Mikiyas Solomon, Tirfe Natnael Ayicheluhem

School of Mechanical and Electrical Engineering, University of Electronic Science and Technology of China, Chengdu 611731, China

***Corresponding Author:** Hongtao Wang, E-mail address: dzkdmdb@163.com*

Abstract:
In the engineering, to ensure the quality and safety, it is necessary to carry out reliability analysis on it. When conducting reliability analysis in engineering, a large number of small failure probability problems will be encountered. For such problems, the traditional Monte Carlo method needs a lot of samples, and the calculation efficiency is extremely low, while the subset simulation method can efficiently estimate the reliability index of the small failure probability problem with little samples. Therefore, this paper takes the application of the subset simulation method in the reliability analysis of the small failure probability structure as the object, constructs the reliability analysis method of the single failure mode of the system, and applies the method to a mathematical example and a single-story gate. Through the rigid frame example, it can be seen that this method is beneficial to improve the calculation efficiency and accuracy.

Keywords: *subset simulation; small failure probability; failure mode; reliability analysis*

1 Introduction

Reliability engineering [1] is a comprehensive engineering discipline that includes various engineering technologies, including statistics and analysis of product failures and their probability of occurrence, reliability design [2-3], reliability prediction [4-6], reliability test [7], reliability evaluation [8-9], reliability inspection [10-11], reliability control [12], reliability maintenance [13-14] and failure analysis [15-17]. Its essence is to fight against failure or malfunction, throughout the whole life cycle of the product. For a product, the high reliability of the system is particularly important. In the engineering system, because all parts work with each other, if some parts fail, it will usually cause serious accidents [18-21]. Therefore, when designing such a system, it needs to have a low failure probability to guarantee that the engineering system has higher safety. For example, in the field of aviation and aerospace, the British Aviation Commission stipulates that the failure rate of aircraft must be lower than 10-5 [22-23]. In the field of automobile industry, there is a key index in the process of automobile design, that is, the safety of automobile structure. According to the design standard of automobile fatigue reliability, the failure probability of key structure of car body should be less than 0.01% [24-25]. Therefore, to achieve high-precision evaluation, it is necessary to study the analysis method of Small Failure Probability (SFP) problem [26-27].

SFP means that the probability of part failure is very small. So it is almost impossible to occur in one test.

However, it will inevitably occur in repeated tests. The reliability analysis method of SFP problem is mainly sampling method [28-29]. The Monte Carlo Simulation (MCS) method has strong versatility, the calculation accuracy increases with the increase of the sampling point capacity. Reliability analysis results with the required accuracy can be obtained theoretically. However, when the dimension of the random variable is too large, the vast majority of the sample points extracted by the MCS method will fall into the safety domain of the design space, which makes little contribution to the reliability analysis of failure events. In addition, the computational cost of obtaining sample points for high-dimensional and highly nonlinear systems is high, which leads to the low efficiency of the MCS method. If the utilization rate of sample points can be improved, especially in the analysis of multi-disciplinary complex systems, the calculation cost will be greatly reduced. For SFP problems in large and complex engineering systems, the subset simulation method (SS) can maintain considerable accuracy and efficiency in calculations [30-32]. SS is an efficient and accurate method for calculating SFP. Its core is to use adaptive method to decompose the whole large probability space into a series of nested subspaces. These

Copyright © 2022 by author(s) and Viser Technology Pte. Ltd. This is an Open Access article distributed under the terms of the Creative Commons Attribution-NonCommercial 4.0 International License (http://creativecommons.org/licenses/by-nc/4.0/), permitting all non-commercial use, distribution, and reproduction in any medium, provided the original work is properly cited.

Received on February 18, 2022; Accepted on May 5, 2022

subspaces are regarded as intermediate failure events, which correspond to a series of conditional failure probabilities. According to Bayesian formula [33-35], these conditional failure probabilities are multiplied in turn, then the tiny failure probability of the required solution is obtained. This method improves the efficiency and accuracy of the SFP problem [36-38].

Abdollahi and Moghaddam et al [39]. introduced the Subset Control Variable (SCV) technology, which is a new method to reformulate the traditional SS and provides statistical features. Au and Beck [40] expressed the failure probability as the product of the larger conditional failure probability, and proposed a new simulation method SS to calculate the SFP encountered in the reliability analysis of engineering systems. Xiao and Zhang et al. [41] proposed an effective Kriging-based Subset Simulation (KSS) method for mixed reliability analysis under random and interval variables using SFP. Qian and Li et al. [42] proposed a time-varying system reliability analysis method, combining multi-response Gaussian process (MRGP) and SS to solve the SFP issues.

The structure of this article can be summarized as follows: The second section reviews the Markov chain Monte Carlo method (MCMC). The third section introduces the principle and calculation process of the SS. In the fourth section, two examples are used to verify the advantages of the SS in solving the SFP. Finally, the content of the full text is summarized in the fifth section.

2 Review of Markov Chain Monte Carlo

MCS [43] is a calculation method based on random numbers. Assuming that the domain of the random variable x is X, and its probability density function (PDF) is f(x). the objective of MCS is to solve the mathematical expectation $E_{f(x)}[g(x)]$. g(x) is the function defined on X. MCS independently samples n samples $x_1, x_2, \cdots \cdots x_n$ according to g(x), the approximate expectation is:

$$E_{f(x)}[g(x)] \approx \frac{1}{n}\sum_{i=0}^{n} g(x_i) \tag{1}$$

Assuming that the integral of solution z(x) on X is required:

$$\int_X z(x)dx \tag{2}$$

It is necessary to decompose z(x) into the g(x) and f(x), and then transform the problem into solving the mathematical expectation $E_{f(x)}[g(x)]$ of the g(x) about f(x):

$$\int_X z(x)dx = \int_X \frac{z(x)}{f(x)} f(x)dx = \int_X g(x)f(x) = E_{f(x)}[g(x)] \tag{3}$$

Then

$$\int_X z(x)dx = E_{f(x)}[g(x)] \approx \frac{1}{n}\sum_{i=0}^{n} g(x_i) \tag{4}$$

In many cases, the performance function z(x) of the system structure is complex and can't be directly used to calculate the failure probability, and the above-mentioned MCS can better solve this problem. However, sometimes the decomposed PDF g(x) is equally complex, and MCS is no longer applicable.

MCMC [44] can efficiently generate a series of samples that obey the complex distribution f(x). Suppose the state space of Markov chain (MC) $(X = X_0, X_1, \ldots, X_t, \ldots)$ is S. Moreover, the transition probability matrix is $P = (P_{ij})$, where P_{ij} denotes the probability that the jth state will be transferred to the ith state. If there is a distribution π=(π1, π2,…)T on the state space S, such that π=Pπ, then the stationary distribution of MC is π.

If an original distribution is the stationary distribution of the MC, after any transfer operation, its result is still the stationary distribution. If the MC is aperiodic, irreducible, and returns normally, its stationary distribution π=(π1, π2,…)T is unique, and its limit distribution is the stationary distribution. According to the ergodic theorem, no matter what the initial distribution π′ is, after n transitions, that is $P^n\pi'$, it will eventually converge to its stationary distribution π, that is:

$$\lim_{t\to+\infty} P(X_t = i|X_0 = j) = \pi_i \; i \in N^+; j \in N^+ \tag{5}$$

For any time t and any state i, j ∈S, the state distribution satisfies the following equation:

$$P(X_t=i|X_{t-1}=j)\pi_j = P(X_{t-1}=j|X_t=i)\pi_i, i,j \in N^+ \tag{6}$$

or abbreviated as:

$$p_{ji}\pi_j = p_{ij}\pi_i, i, j \in N^+ \tag{7}$$

This is the meticulous equilibrium equation.

The core idea of MCMC method is divided into the following 3 steps. Firstly, define an MC π=(π1, π2,…)T in the state space S of the random variable X to make its stable distribution as the sampling target distribution f(x). Secondly, randomly walk on this MC to get a sample at any time. Thirdly, find the mathematical expectation of the function according to the ergodic theorem. The meaning of the ergodic theorem is as follows: if the time tends to infinity and the sample distribution closes a stationary distribution, then the function mean of the sample is close to the mathematical expectation of the function.

In this paper, Metropolis-Hastings algorithm [45], is adopted to define MC and transition kernel. Suppose a probability distribution that needs to be sampled is f(x)

$$p(x, x') = t(x, x')\beta(x, x') \tag{8}$$

where x′ represents the candidate state; β(x, x′) is called the accepted distribution; t(x, x′) represents the transfer core of another MC; and it is called the suggested distribution.

$$\beta(x, x') = \min\left\{1, \frac{p(x')t(x', x)}{t(x, x')p(x)}\right\} \tag{9}$$

Since

$$\begin{aligned} p(x)t(x, x') &= p(x)t(x, x')\min\left\{1, \frac{p(x')t(x', x)}{t(x, x')p(x)}\right\} \\ &= \min\{t(x, x')p(x), t(x', x)p(x')\} \\ &= t(x', x)p(x')\min\left\{1, \frac{t(x, x')p(x)}{t(x', x)p(x')}\right\} \\ &= p(x', x)p(x') \end{aligned} \tag{10}$$

satisfies the meticulous equilibrium equation. The transition kernel $p(x', x)$ satisfies the ergodic theorem and the final stationary distribution is $p(x)$, that is, the samples generated in this way conform to the $p(x)$ distribution.

It is suggested that $t(x, x')= t(x', x)$, then

$$\beta(x, x') = \min\left\{\frac{p(x')}{p(x)}, 1\right\} \tag{11}$$

Particularly, $t(x, x') = t(|x - x'|)$ is called the random walk Metropolis algorithm, such as the normal distribution transition kernel:

$$t(x, x') \propto \exp\left(-\frac{(x'-x)^2}{2}\right) \tag{12}$$

Its characteristic is that when x' is closer to the mean value x, the acceptance probability is higher.

The steps of Metropolis-Hastings algorithm are:

Ⅰ. According to the objective distribution function $f(x)$ to be sampled, select a suggested distribution $t(x, x')$ and randomly select an initial value $x = x_0$;

Ⅱ. According to the recommended distribution $t(x, x')$, a candidate state x' is randomly selected and the acceptance probability is calculated :

$$\beta(x, x') = \min\left\{1, \frac{p(x')t(x', x)}{t(x, x')p(x)}\right\} \tag{13}$$

Ⅲ. A number m is randomly selected from interval (0, 1) according to uniform distribution. If $m \leq \beta(x, x')$, then accept the candidate state x', otherwise, refuse to transfer.

In the SS of this paper, the candidate state x' newly generated by MCMC must meet the conditions $x' \in F_i$, to ensure that the newly generated state is within the failure domain F_i area.

3 Subset simulation method

SS is a random simulation process for estimating SFP. Specifically, consider an engineering system constrained by random input parameters. The failure area E is defined as the sub-area of the response function $G(x)$ less than a certain threshold b in x space, that is:

$$E = \{x: G(x) < b\}\# \tag{14}$$

where x represents the random input vector of all uncertain parameters. In the SS, $G(x)$ can be a nonlinear implicit function of x. In many cases, the target failure probability PE related to the target failure event E may be small, so it is necessary to carry out much simulation to estimate the target failure probability to obtain the required accuracy, but it also reduces the computational efficiency. The SS method transforms an SFP into a product of a larger conditional probability sequence. This transformation method is to divide the input parameter space into subsets of fault domains. Therefore, it is necessary to define a series of intermediate failure events in the same way as the target failure event

$$E_j = \{x: G(x) < b_j\}, j = 1, \dots, m \tag{15}$$

where m represents the total number of intermediate events, and b_j represents a set of thresholds of the system response function. Suppose $E_1, E_2, \dots, E_m$ is a nested event sequence, that is, $E_1 \supset E_2 \supset \dots \supset E_2 = E$, but the value of b_j cannot be predetermined. However, setting the conditional probability $P(E_j|E_{j-1})$ equal to a specified value. To ensure the nesting of E_j, set the threshold value as $b_1 > b_2 > \dots > b_m = 0$. Because all intermediate events are nested, then

$$P_E = P(E_1)\prod_{j=2}^{m} P(E_j|E_{j-1}) \tag{16}$$

In the reliability analysis, the SS starts from the first step, and the probability P1 related to the first intermediate event E_1 is calculated as follows:

$$P_1 = P(E_1) \approx \frac{1}{N}\sum_{i=1}^{N} I_{E_1}(G(x_i)) \tag{17}$$

where N denotes the total number of samples of the first intermediate event, that is, the first simulation layer; $\{x_i\}$ represents a random input vector sequence of all uncertain parameters in the system generated according to known PDF, which is an independent and identically distributed sample. $I_{E_1}(\cdot)$ is an index function:

$$I_{E_1}(\cdot) = \begin{cases} 0 & \text{if}(x_i) \geq b_1 \\ 1 & \text{if}(x_i) < b_1 \end{cases} \tag{18}$$

where the first intermediate event and its threshold are unknown, but if the conditional probability of each layer is set to a fixed value p_1, the values of threshold b_1 and first intermediate event E_1 can be determined according to Eq. (17). After generating $\{x_i\}$, all N system response functions $\{G(x_i)\}$ are calculated and sorted in ascending order so that $G(x_1) \leqslant G(x_2) \leqslant \cdots \leqslant G(x_N)$. Let b_1 be the sample quantile of the system response function in the first layer simulation, that is $b_1 = G(x_{[P_1 N]})$, then samples $x_1, x_2, \dots, x_{[P_1 N]}$ all belong to the first intermediate event E_1.

In the subsequent intermediate event E_j, the sample source is the previous intermediate event E_{j-1}. Considering that there are already $[N \times P_{j-1}]$ samples that belong to E_{j-1}, you can use the sampling method based on MCMC to get the required conditional samples $\{x_i\}$. Then use $P(E_j|E_{j-1})$ to perform probability estimation on the simulation layer:

$$P_j = P(E_j|E_{j-1}) \approx \frac{1}{N}\sum_{i=1}^{N} I_{E_j}(G(x_i)) \tag{19}$$

where the sample $x_i \in f(x|E_{j-1}), i = 1, \dots, N$ is produced by MCMC. Generate $N - [N \times P_{j-1}]$ conditional samples in the intermediate event E_{j-1} and combine them with the previously selected $[N \times P_{j-1}]$ samples. All N system response functions $\{G(x_i)\}$ can be calculated, and sorted in ascending order. Let b_j be the sample quantile of N system response values in event E_j, namely $b_j = G(x_{[P_j N]})$. In this way, $x_1, x_2, \dots, x_{[P_j N]}$ all belong to intermediate event E_j.

Iterate the above steps repeatedly. When the sample quantile of N system response values in space E_{j-1} below b, that is $b_j = G(x_{[P_j N]}) < b$, stop the iteration. At this point, the SS algorithm has reached the target failure

domain E_m, that is, $j = m$ and $b_m = b$. The final conditional probability estimates of $P(E_m|E_{m-1})$ is:

$$P(E_m|E_{m-1}) \approx P_m = \frac{1}{N}\sum_{i=1}^{N} I_{E_m}(G(x_i))\# \quad (20)$$

Combining Eq. (16), (17), (18) and (19)

$$P_E = \prod_{j=1}^{m} P_j \quad (21)$$

In the practical application, the value of P_j, $j = 1, \ldots, m$ are usually $P_j = p_0 \in (0.1 \sim 0.3)$.

Therefore, the steps of applying SS in MATLAB can be briefly summarized as follows: Ⅰ. Define the algorithm parameters; Ⅱ. Using direct MCS to generate the first intermediate failure event; Ⅲ. Using MCMC method to generate the remaining intermediate failure events; Ⅳ. Calculate the failure probability of the target event by multiplying the conditional probabilities of all intermediate failure events.

The algorithm flow is shown in Figure 1:

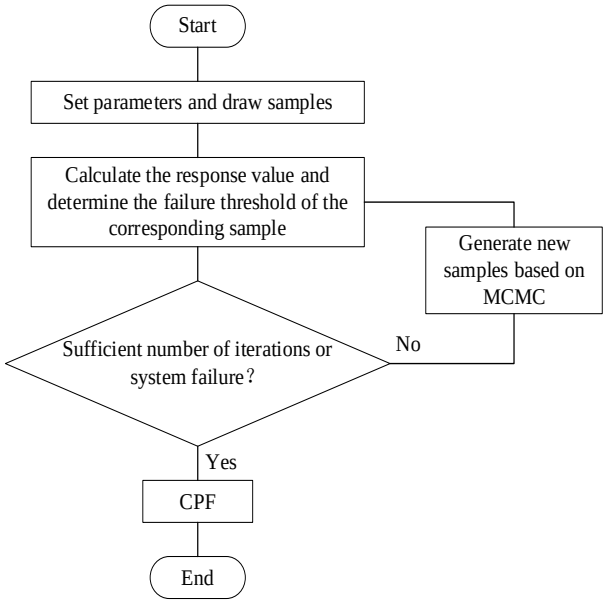

Figure 1 The flow chart of SS algorithm

4 Examples

4.1 The example 1

The functional function of the mathematical example has been given:

$$G(x) = 0.0185361 - \frac{73.8221x_1}{x_2^3} \quad (22)$$

where $x_1 \sim N(1100,201.5)$, $x_2 \sim N(253,38.1)$, the failure mode is that the value of the function is below 0.

Use SS to calculate its reliability. In the setting of basic parameters, the total number N of samples is 2000, and the conditional probability of each simulation layer is set to p_0=0.25. By running the MATLAB program based on SS, the consequences are shown in Table 1:

Table 1 shows the whole process of calculating the failure probability of the system response function by MATLAB. The program has implemented three random simulation layers, including one MCS layer (j=1) and two MCMC simulation layers (j=2, 3). The basis for stopping the cycle of this program is to judge the quantile of the current analog layer sample $g(x_{[P_jN]})$ is less than zero. Of course, the third simulation layer meets this criterion and reaches the failure zone of the system failure mode, so the program exits the loop. Then, it is found that the number of all samples in the simulation layer whose response value is less than zero is 540, so the failure probability of the response function is 9.2×10-3, and a total of 2000+1500+1500=5000 random samples are needed.

Table 1 The execution process of SS

Simulation layer j	Seed number N_j	Number of samples generated in layer j N-Nj	Condition P(U(j+1)|U(j))	The failure mode probability obtained by the J layer
0	0	2000		
1	500	1500	0.25	
2	500	1500	0.25	
3	540		0.27	P(E1)=9.0×10-3

For the rigor of the experiment, this paper also uses MCS to verify the accuracy of the result. After many attempts, it is found that the failure probability of the response function converges only when the total number of selected samples is above 105. The number of samples below this order of magnitude will affect the accuracy of the results, while the number above this order of magnitude will greatly affect the calculation efficiency. Therefore, we choose to randomly generate 200,000 samples in the whole sample space according to the standard normal distribution and calculate all the corresponding response function values, and find out the total number of samples whose response value is less than zero, and the ratio of the total number to 200,000 is the required failure probability value. The comparison consequences are shown in Table 2.

Table 2 Comparison of two methods

Analogy procedure	Failure probability	Total number of samples required
SS	9.0×10-3	5000
MCS	9.5×10-3	200000

Use MATLAB to draw the cumulative distribution curve of the response function. It is shown in Figure 2 and Figure 3.

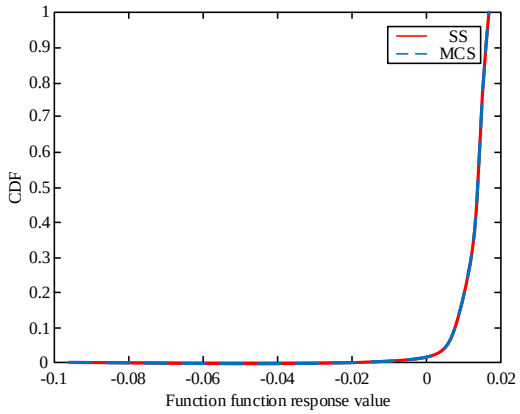

Figure 2 The CDF curve (a)

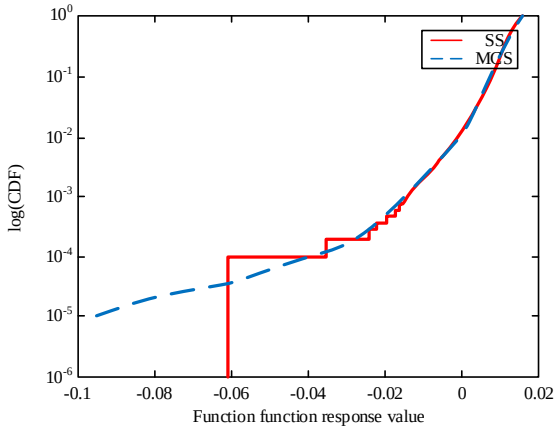

Figure 3 The CDF curve (b)

The results calculated by SS are represented by red real lines, and the results calculated by MCS are represented by blue virtual lines. It can be seen that the result of SS fits well with that of direct MCS, and it can be found from semi-logarithmic coordinate Figure 3 that the SS can also accurately fit the part with SFP. Only after the order of magnitude is 10-4 will there be a significant difference. Therefore, it can be concluded that while ensuring a certain accuracy, the SS only needs 5000 samples to accurately calculate the failure probability of the failure mode corresponding to the response function, while the direct MCS needs dozens or even hundreds of samples. Therefore, the application of SS in SFP problem can greatly improve the computational efficiency and save computational resources.

4.2 The example 2

Calculate the reliability of the single-layer portal frame structure as shown in the Figure 4. The elastic modulus values of beams and columns are both taken as: $E=2\times10^{6}\,\mathrm{kN/m^2}$. There is a correlation between the section moment of inertia and the section area: $I_i=a_iS_i^2$. F is the load variable, S1 and S2 respectively represent the cross-sectional area of the beam and column, and the statistical information of each random variable is shown in Table 3. The response of the structure is taken as the displacement value of the top layer of the rigid frame, and the displacement limit of the structure is 0.01m, then the performance function of the structure based on displacement is:

$$Z=g(X)=0.01-u(X) \tag{22}$$

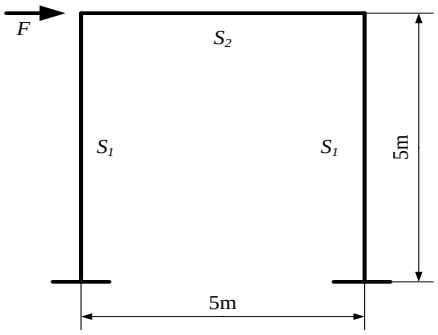

Figure 4 The schematic diagram of single-layer portal frame

Table 3 The information of random variables

Basic variables	Distribution type	Mean	Standard deviation	αi
A1	Lognormal	0.34	0.034	0.08234
A2	Lognormal	0.16	0.016	0.16333
P	Extreme value type Ⅰ	20	5.0	--

In this section, the rod system model in the OpenSees software is used to simulate the plane rigid frame, and the beams and columns are taken as the basic elements.

This section considers the correlation between A1 and A2. The nonlinear correlation coefficient τk is set to 0.0 and 0.3, respectively, and the SS is used for reliability analysis. At the same time, the failure probability and reliability index obtained by MCS for 100,000 simulations are compared with the SS, as shown in Table 4.

From Table 4 can know that the SS greatly reduces the number of calculations and obtains more accurate and reliable indicators. As shown in Figure 5, through the cumulative distribution curve of the performance function, it can be seen that the curve fitting degree of the SS and the MCS method is better. In the semi-logarithmic coordinates, it can be seen that the cumulative distribution curve only has a significant difference after the order of magnitude is 10-4.

In the process of applying the SS, when the number of selected samples N and the conditional probability P0 are different, the calculated results are different. The number of samples is N=100, 200, 500, 1000; the conditional probability is P0=0.1, 0.2, 0.3, 0.4. Draw the cumulative distribution function curve, as shown in Figure. 6. The difference can almost be bridged with MCS for 100,000 times.

Table 4 The result analysis and comparison

Correlation coefficient	Method	Reliable indicators	Probability of failure	Total sample points	Time (s)
τk=0.0	MCS	2.7910	2.130×10-3	100000	14382
	SS	2.7994	2.060×10-3	450	74
τk=0.3	MCS	3.0842	9.875×10-4	100000	13985
	SS	3.0210	5.182×10-4	500	91

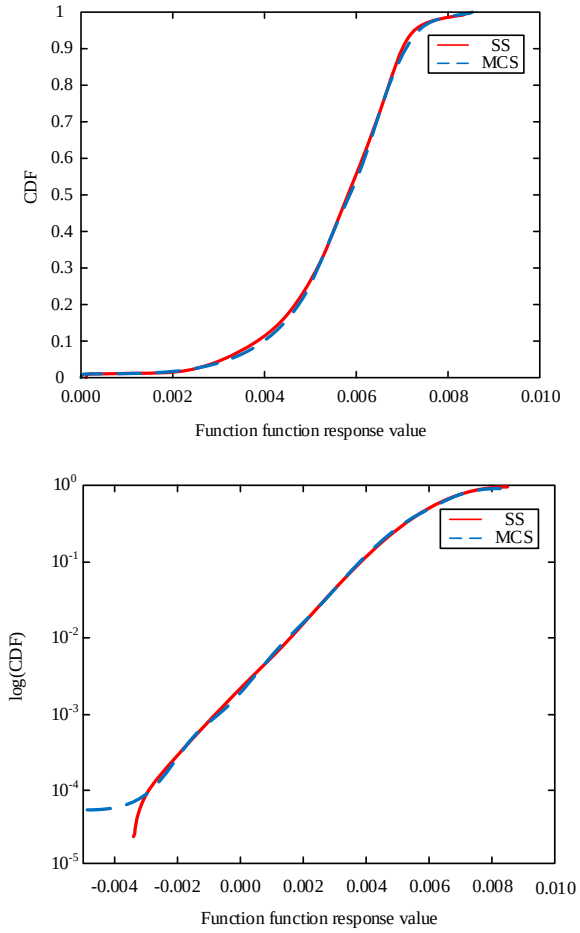

Figure 5 The CDF curve of performance function of portal frame

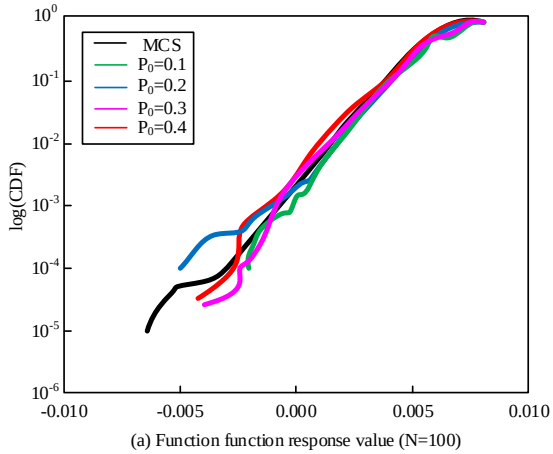

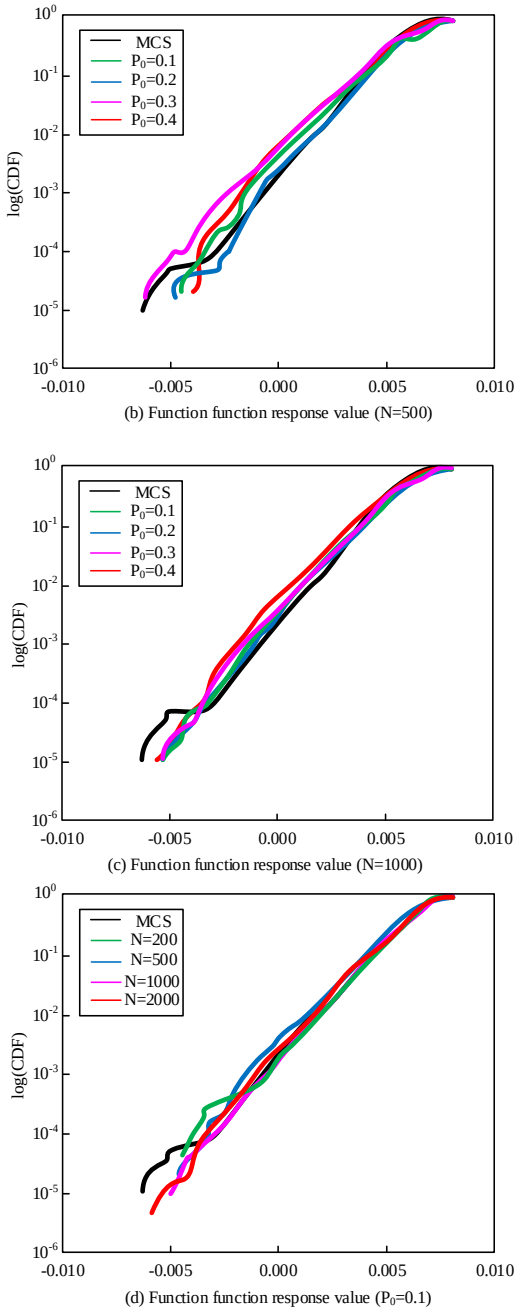

Figure 6 The CDF curve of different initial sample points and failure probability combination

In Figure 6 (a), (b), (c), as the initial number of samples increases, the curve tail fitting becomes more accurate. It can be seen that the more the number of initial sample points, the better the simulation probability of a smaller range of points. When the initial sample points are small, the sample points with small occurrence probability will be ignored. For the selection of the conditional failure probability, when a smaller conditional probability is selected, the simulation curve of the SS and the curve of the MCS fit better, but the number of calculation subsets increases and the calculation efficiency decreases. It can be seen that the selection of

appropriate initial sample points and conditional failure probability has a certain impact on the accuracy and efficiency of the SS.

5 Conclusion

Aiming at the calculation of SFP in reliability analysis of engineering system, this paper discusses it based on SS. The SS adaptively extracts samples by applying MCMC method, and divides the whole probability space into a series of nested subspaces, which makes the subspaces approach to the failure area continuously. Therefore, the SFP of the target event can be accurately forecasted with a relatively small number of samples, and the calculation efficiency is improved. The reliability assessment method based on SS is constructed, and the analysis method is realized in two examples, which verifies the effectiveness of the proposed method. Then, this method is used in the engineering example to analyze the reliability problem.

Acknowledgments

This research was funded by the Sichuan Science and Technology Innovation Seedling Project Funding Project (Grant No. 2021112).

References

[1] Modarres M, Kaminskiy M P, Krivtsov V, 2016. Reliability engineering and risk analysis: a practical guide. CRC press.

[2] Huang Z L, Jiang C, Zhang Z, et al., 2019. Evidence-theory-based reliability design optimization with parametric correlations. Structural and Multidisciplinary Optimization, 60(2): 565-580.

[3] Huang Z L, Jiang C, Zhang Z, et al., 2017. A decoupling approach for evidence-theory-based reliability design optimization. Structural and Multidisciplinary Optimization, 56(3): 647-661.

[4] Sahu K, K Srivastava R, 2020. Needs and importance of reliability prediction: An industrial perspective. Information Sciences Letters, 9(1): 5.

[5] BahooToroody A, De Carlo F, Paltrinieri N, et al., 2020. Bayesian regression based condition monitoring approach for effective reliability prediction of random processes in autonomous energy supply operation. Reliability Engineering & System Safety, 201: 106966.

[6] Cheng Y, Zhu H, Hu K, Wu J, et al., 2019. Reliability prediction of machinery with multiple degradation characteristics using double-Wiener process and Monte Carlo algorithm. Mechanical Systems and Signal Processing, 134:106333.

[7] Aslam M, 2019. A new failure-censored reliability test using neutrosophic statistical interval method. International Journal of Fuzzy Systems, 21(4):1214-1220.

[8] Fan C L, Song Y, Lei L, et al., 2018. Evidence reasoning for temporal uncertain information based on relative reliability evaluation. Expert Systems with Applications, 113:264-276.

[9] Meng D, Yang S, Zhang Y, et al., 2019. Structural reliability analysis and uncertainties - based collaborative design and optimization of turbine blades using surrogate model. Fatigue & Fracture of Engineering Materials & Structures, 42(6) 1219-1227.

[10] Liu Y, Zuo M J, Li Y F, et al., 2015. Dynamic reliability assessment for multi-state systems utilizing system-level inspection data. IEEE Transactions on Reliability, 64(4):1287-1299.

[11] Lu L, Anderson-Cook C M, 2017. Choosing a reliability inspection plan for interval censored data. Quality Engineering, 29(3):512-535.

[12] Grishko A, Adnreev P, Goryachev N, et al., 2018. Reliability control of complex systems at different stages of their life cycle. In 2018 Ural Symposium on Biomedical Engineering, Radioelectronics and Information Technology (USBEREIT) (pp. 220-223).

[13] De Almeida A T, Ferreira R J P, Cavalcante, C A V, 2015. A review of the use of multicriteria and multi-objective models in maintenance and reliability. IMA Journal of Management Mathematics, 26(3):249-271.

[14] De Almeida A T, Cavalcante C A V, Alencar M H, et al., 2015. Multicriteria and multiobjective models for risk, reliability and maintenance decision analysis (Vol. 231). New york: Springer International Publishing.

[15] Abdullah L, Singh S S K, Azman A H, et al, 2019. Fatigue life-based reliability assessment of a heavy vehicle leaf spring. International Journal of Structural Integrity, 10(5):726-736.

[16] Liu X, Zhang Y, Xie S, et al., 2021. Fatigue failure analysis of express freight sliding side covered wagon based on the rigid-flexibility model. International Journal of Structural Integrity, 12(1):98-108.

[17] Li S, Liu X, Wang X, et al., 2020, Fatigue life prediction for automobile stabilizer bar. International Journal of Structural Integrity, 11(2):303-323.

[18] Nahal M, Khelif R, 2021. A finite element model for estimating time-dependent reliability of a corroded pipeline elbow. International Journal of Structural Integrity, 12(2):306-321.

[19] Abd Rahim A A, Abdullah S, Singh S S K, et al., 2019. Reliability assessment on automobile suspension system using wavelet analysis. International Journal of Structural Integrity, 10(5): 602-611.

[20] Meng D, Wang H, Yang S, et al., 2022. Fault analysis of wind power rolling bearing based on EMD feature extraction. CMES-Computer Modeling in Engineering & Sciences, 130(1): 543-558.

[21] Yang S, Wang J, Yang H, 2022. Evidence theory based uncertainty design optimization for planetary gearbox in wind turbine. Journal of Advances in Applied & Computational Mathematics, 9: 86-102.

[22] Yang Y M, Yu H, Sun Z, 2017. Aircraft failure rate forecasting method based on Holt-Winters seasonal model. In 2017 IEEE 2nd International Conference on Cloud Computing and Big Data Analysis (ICCCBDA), (4):520-524).

[23] Yang Y, Zheng H, Zhang R, 2017. Prediction and analysis of

aircraft failure rate based on SARIMA model. In 2017 2nd IEEE International Conference on Computational Intelligence and Applications (ICCIA) (pp. 567-571).

[24] Wang B J, Li Q, Ren Z S, et al., 2020. Improving the fatigue reliability of metro vehicle bogie frame based on load spectrum. International Journal of Fatigue, 132:105389.

[25] Kong Y S, Abdullah S, Schramm D, et al., 2019. Development of multiple linear regression-based models for fatigue life evaluation of automotive coil springs. Mechanical Systems and Signal Processing, 118:675-695.

[26] Yun W, Lu Z, Jiang X, 2018. An efficient reliability analysis method combining adaptive Kriging and modified importance sampling for small failure probability. Structural and Multidisciplinary Optimization, 58(4):1383-1393.

[27] Xiao N C, Zhan , Yuan K, 2020. A new reliability method for small failure probability problems by combining the adaptive importance sampling and surrogate models. Computer Methods in Applied Mechanics and Engineering, 372, 113336.

[28] Zhang J, Xiao M, Gao L, et al., 2019. A combined projection-outline-based active learning Kriging and adaptive importance sampling method for hybrid reliability analysis with small failure probabilities. Computer Methods in Applied Mechanics and Engineering, 344:13-33.

[29] Gong W, Juang C H, Martin J R, et al., 2016. New sampling method and procedures for estimating failure probability. Journal of Engineering Mechanics, 142(4):04015107.

[30] Meng D, Yang S, Lin T, et al., 2022. RBMDO using gaussian mixture model-based second-order mean-value saddlepoint approximation. CMES-Computer Modeling in Engineering & Sciences, 132(2): 553-568.

[31] Pan Q, Dias D, 2017. An efficient reliability method combining adaptive support vector machine and Monte Carlo simulation. Structural Safety, 67:85-95.

[32] Hsu W C, Ching J, 2010. Evaluating small failure probabilities of multiple limit states by parallel subset simulation. Probabilistic Engineering Mechanics, 25(3):291-304.

[33] Meng D, Yang S, de Jesus A M, Zhu S P, 2022. A novel Kriging-model-assisted reliability-based multidisciplinary design optimization strategy and its application in the offshore wind turbine tower. Renewable Energy. https://doi.org/10.1016/j.renene.2022.12.

[34] Yang Z, Kan Y, Chen F, et al., 2015. Bayesian rel Chinese Journal of Mechanical Engineering, 28(6):1229-1239.

[35] Yuan R, Tang M, Wang H, et al., 2019. A reliability analysis method of accelerated performance degradation based on bayesian strategy. IEEE Access, 7:169047-169054.

[36] Meng D, Yang S, de Jesus A M, Zhu S P, 2022. A novel Kriging-model-assisted reliability-based multidisciplinary design optimization strategy and its application in the offshore wind turbine tower. Renewable Energy. https://doi.org/10.1016/j.renene.2022.12.

[37] Li H S, Ma Y Z, Cao Z, 2015. A generalized Subset Simulation approach for estimating small failure probabilities of multiple stochastic responses. Computers & Structures, 153:239-251.

[38] Huang X, Chen J, Zhu H, 2016. Assessing small failure probabilities by AK–SS: An active learning method combining Kriging and Subset Simulation. Structural Safety, 59:86-95.

[39] Abdollahi A, Moghaddam M A, Monfared S A , et al., 2020. A refined subset simulation for the reliability analysis using the subset control variate. Structural Safety, 87:102002.

[40] Au S K, Beck J L, 2001. Estimation of small failure probabilities in high dimensions by subset simulation. Probabilistic engineering mechanics, 16(4):263-277.

[41] Xiao M, Zhang J, Gao L, et al., 2019. An efficient Kriging-based subset simulation method for hybrid reliability analysis under random and interval variables with small failure probability. Structural and Multidisciplinary Optimization, 59(6):2077-2092.

[42] Qian H M, Li Y F, Huang H Z, 2021. Time-variant system reliability analysis method for a small failure probability problem. Reliability Engineering & System Safety, 205:107261.

[43] Meng D, Yang S, He C, et al., 2022. Multidisciplinary design optimization of engineering systems under uncertainty: a review. International Journal of Structural Integrity, 13(4), 565-593.

[44] Van Ravenzwaaij D, Cassey P, Brown S D, 2018. A simple introduction to Markov Chain Monte–Carlo sampling. Psychonomic bulletin & review, 25(1):143-154.

[45] Jensen H A, Jerez D J, Valdebenito M, 2020. An adaptive scheme for reliability-based global design optimization: A Markov chain Monte Carlo approach. Mechanical Systems and Signal Processing, 143:106836.

Viser Technology Pte. Ltd.
Mechanical Engineering Science
DOI: 10.33142/mes.v4i1.7513

Research Article Open Access

Topology optimization design of the main structure of 6-DOF manipulator based on the variable density method

Yujian RUI[1],Yongming LIU[1*],Zhen ZHANG[1], Zhijian TU[2], Jian WU[3], Neng WEI[2],Zhuanzhe ZHAO[1*]

1. School of Mechanical Engineering, Anhui Polytechnic University, Anhui Wuhu 241000, China
2. Wuhu Ceprei Robotics Industry Technology Institute Co., Ltd., Anhui Wuhu 241000, China
3. Wuhu Institute of Technology, Anhui Wuhu 241000, China

***Corresponding Author:** Yongming LIU, Wuhu, 241000, China, liuyongming1015@163.com; Zhuanzhe Zhao, Wuhu,241000, China, zhuanzhe727@ahpu.edu.cn*

Abstract:
In order to solve the problems of too large mass, too complex structure and poor flexibility of the 6-DOF manipulator, the topological optimization theory based on variable density method is applied to the 6-DOF manipulator, the topology optimization of the main structural components of the manipulator is carried out with the help of the finite element software ANSYS, and the optimized structure is simplified according to the density distribution of the units and the requirements of manufacturability, the results are compared and analysed by static mechanics. It shows that the whole mass of the 6-DOF manipulator is reduced by 47.23% without changing the original mechanical properties after topological optimization, and the optimized model can meet the requirements of manufacturability, the optimization effect is significant, which can be used as a reference for the structure optimization of the 6-DOF manipulator.

***Keywords:** Variable density method; topology optimization; 6-DOF manipulator; finite element analysis*

Introduction

Six-degree-of-freedom manipulators are widely used in the field of industrial robots. As the executing mechanism of the robot, the tiny deformation of the components of the robot arm is related to its control accuracy, and the stress state of the material will affect the service life of the robot arm, the change of these factors will make the overall use of the robot effect changes. The structural optimization of 6-DOF arms mostly depends on the manufacturing experience of engineers, and the theory of topology optimization is seldom used.

Topology optimization is to get the best distribution scheme and the best load-transfer path in a given design space, taking the material distribution as the optimal objective function. The concept of topology optimization, which originated from the problem of structural design, has now been widely applied in many fields, such as heat [1], fluid mechanics [2], acoustics [3], electromagnetism [4], optics [5] and the combination of multiple disciplines. At present, the common methods of Continuum topology optimization are variable density method [6], evolutionary structural optimization method [7], level set method [8] and so on.

In order to solve the problems of the 6-DOF manipulator which is too heavy and the fuselage structure is too complex, the variable density topology optimization method is used to carry on the topology optimization analysis in ANSYS software, the structure of the manipulator is optimized reasonably, and then the optimized model is re-introduced into the ANSYS software according to the optimized cloud chart, and the stress, stress and deformation are analyzed and compared, thus realizes to the main body structure supplement optimization.

1 Topology optimization theory based on variable density method

The variable density method is a topological optimization method based on the description of the physical properties of isotropic materials, at the same time, it is assumed that the pseudo-density is also the relation between the material density and the material characteristics of each unit and the elastic coefficient. At present, the common interpolation models are penalty

Copyright © 2022 by author(s) and Viser Technology Pte. Ltd. This is an Open Access article distributed under the terms of the Creative Commons Attribution-NonCommercial 4.0 International License (http://creativecommons.org/licenses/by-nc/4.0/), permitting all non-commercial use, distribution, and reproduction in any medium, provided the original work is properly cited.
Received on February 14, 2022; Accepted on May 30, 2022

interpolation model or rational approximation model of material properties [9]. In order to make the intermediate density approach to interval, a penalty factor is introduced to punish the intermediate density, the SIMP method based on variable density theory is adopted. The variable density method has the advantages of high calculation efficiency and easy solution. The mathematical expression is as follows:

$$\rho = X_e \rho_0 \tag{1}$$

Where Xe is the relative density of the elements; ρ0 is the inherent density of each element; and ρ is the topology optimization design variable. When Xe = 1, all structural materials are retained; when Xe = 0, all structural materials are eliminated. Because of the discontinuity of ρ, the design variables must be continuous in topology optimization, and the upper formula must be solved by derivation.

$$K_e = (X_e)^p K_0 \tag{2}$$

Where Ke is the stiffness of the element, K0 is the inherent stiffness of the element and p is the penalty factor. Equation (2) can be written as

$$C(x) = F^T U = U^T F U \tag{3}$$

Where C(x) is the structural compliance; F is the Load Vector; K is the Global Stiffness Matrix; U is the displacement vector. For constrained volume, in order to maximize material stiffness, the topology optimization based on variable density method can be written as

$$\begin{aligned} &Find: \quad x = \{x_1, x_2, x_3 \Lambda\ , x_n\} \\ &Minimize: C(x) = F^T U \\ &Subject\ to: \begin{cases} f = \dfrac{V - V_1}{V_0} \\ 0 \le x_{\min} \le x_e \le x_{\max} \\ F = KU \end{cases} \end{aligned} \tag{4}$$

Where n is the total number of elements; xe is the design variable, which represents the relative density of the e element; v is the volume of the structure before optimization; V0 is the volume of the structure design area; V1 is the volume with density less than 1; $f = \frac{V-V_1}{V_0}$ is the volume constraint equation; xmin is the lower limit of element density and xmax is the upper limit of element density. In order to avoid singularity of stiffness matrix, xmin=0.001. F=KU is a finite element equilibrium equation constraint.

In the variable density topology optimization method, the design variable can take any density value in. When the relation between elastic modulus and relative density is constant, different interpolation modes produce different models. The formula of SIMP method for interpolation model is

$$E(x_i) = E_{\min} + x_i^p (E_0 - E_{\min}) \quad i = 1, \Lambda\ , n \tag{5}$$

Where E is the interpolated modulus of elasticity, E0 is the initial modulus of elasticity, p is the penalty factor, and Emin is the modulus of elasticity of the blank cell, in general, Emin usually takes a minimum value to ensure that the stiffness moment singularity does not occur during the optimization process.

In the process of topology optimization of continuum structures by variable density method, numerical instability often occurs, because the grid division is needed in the pre-processing, in order to avoid the influence of numerical instability on the final optimization results, the sensitivity filtering technique is used in the optimization process. The sensitivity filtration technique is to filter and correct the sensitivity of each unit in the material. The formulas are as follows

$$\frac{\overline{\partial c}}{\partial x_i} = \frac{1}{x_i \sum_{j=1}^{N_i} H_{ij}} \sum_{j=1}^{N_i} H_{ij} x_i \frac{\partial c}{\partial x_i} \tag{6}$$

$$H_{ij} = \max(0, r_{\min} - \Delta(i, j)) \tag{7}$$

Where xi is the sensitivity; rmin is the filter radius; Ni is the number of elements in the filter radius rmin with i as the center; Hij is the weight equation; Δ is the central distance between unit i and Unit j.

The technical route of variable density topology optimization of the main body of the manipulator is shown in Figure 1.

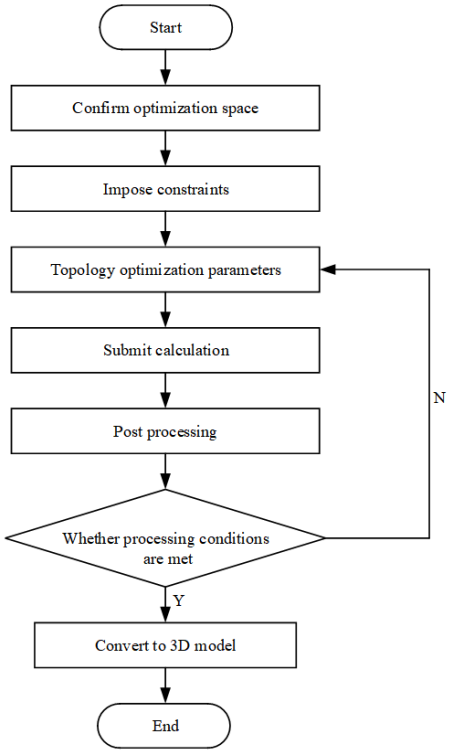

Figure 1 Technical route of topology optimization with variable density method

The topology optimization process is as follows:

(1) Define the design area, determine the material parameters, design the area grid division, determine the

different grid division parameters for the different main structure, determine the space to be optimized;

(2) Establish the correct boundary conditions, determine the load conditions, constraints are imposed;

(3) The parameters of topology optimization are set according to the actual demand;

(4) The parameters are calculated and analyzed;

(5) The updated design variables are compared with the optimization parameters to judge whether they meet the requirements;

(6) Repeat steps 3-5) until the processing conditions are met;

(7) Remodel the optimized structure.

2 Topology optimization design of main parts

The structural optimization design of the 6-DOF manipulator mainly lies in the three parts of the small arm, the big arm and the rotating base, the objective function is set as the compliance of the model, and the mass of the material is defined as a variable in the response constraint of Ansys, and the maximum stress, strain and volume are taken as the constraints.

Ansys Workbench 19.0 software already has a complete topology optimization module, which integrates the objective function and constraints without the need to use the APDL language by itself. For the optimization principle of constant stiffness and volume reduction of the model before and after topology optimization, the same constraints are applied to the model before and after the optimization and the static analysis is performed respectively. The validity of the optimization results can be obtained by comparing the total deformation data before and after optimization. The total deformation data before and after optimization should not change too much.

Table 1 Material properties.

Material	Density [Kg mm-3]	Elasticity modulus [Pa]	Poisson ratio	Tensile strength [Pa]	Yield strength [Pa]
45#	7850	2.1e+11	0.269	6e+8	3.55e+8

2.1 Topology optimization of the small arm

The main control arm of the manipulator vertical up and down two aspects of the displacement, the arm topology optimization design, the quality constraints of 50% , for the optimization of the small arm structure before and after the design as shown in Figure 2.

After topological optimization of the small arm, the density of the part originally connected with the bearing hole is effectively reduced.The overall volume is reduced from 3.499e+5 mm3 to 1.9411e+5 mm3, and the optimized volume is 55.477% of the original volume; The mass is reduced from 2.7467 Kg to 1.5238 Kg, and the optimized mass is 55.477% of the original mass.

As can be seen from the density distribution diagram, the bearing holes of the boom are optimized and reduced, and the overall optimized model is rough and irregular, so that the model can be manufactured later, the simplified model is processed according to the density distribution of the model and the requirement of manufacturing, which makes the simplified model have the same performance as the original structure. The topology optimization module of Ansys, "Spelclaim", is used to obtain a complete 3D model of the optimized model and to modify the optimized model. According to the principle of not changing the density distribution of the model itself after optimization and easy manufacturing and processing, the rough and convex parts of the original optimized model surface are smoothed. The simplified model reconstructed is shown in Figure 3.

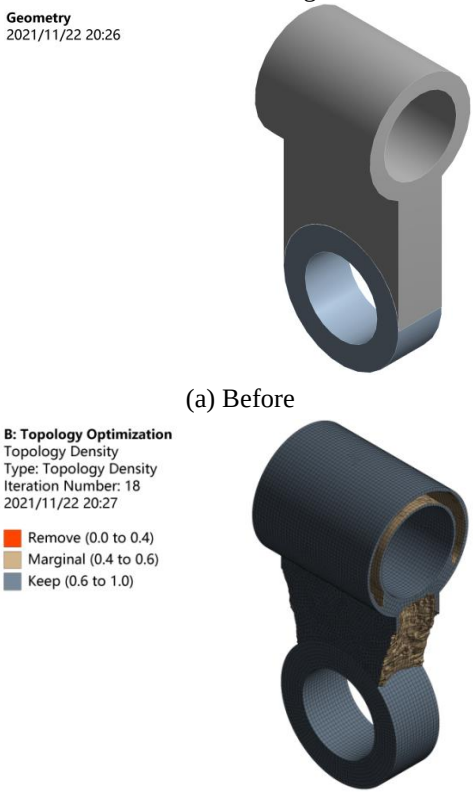

(a) Before

(b) After

Figure 2 Comparison of fore-and-aft optimization of small arm model.

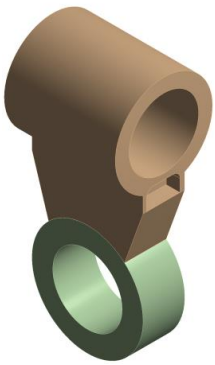

Figure 3 Simplified model of small arm after optimization

The static analysis of the simplified model before and after optimization is carried out under the same conditions. A load of 200 N is applied in the bearing bore, and the type of load action is "BearingLoad", which can better reflect the force distribution in the bearing bore. "BearingLoad" usually adopts the method that the load is distributed on the contact surface of the shaft and the hole according to the sinusoidal law, assuming that the magnitude of the acting force is distributed according to the sinusoid. This method is widely used in practice because of the simple law and good compliance for the simple structure of holes and shafts (The following forces are the same type of load action). The results of the static analysis are shown in Figure 4.

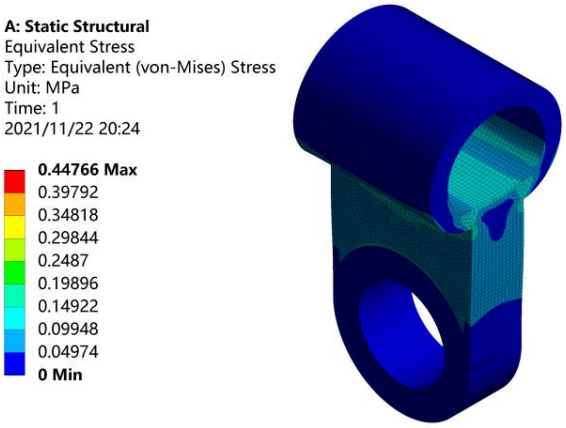

(a) Before

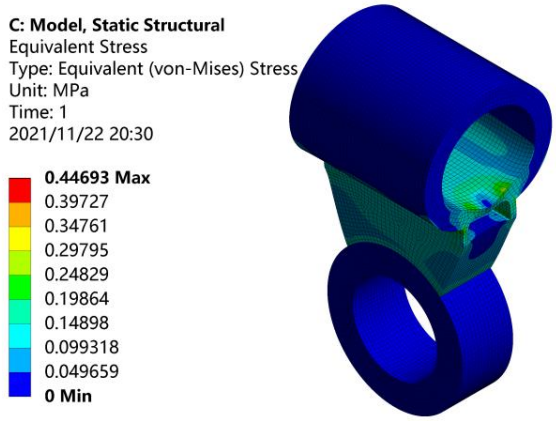

(b) After

Figure 4 Equivalent stress Nephogram of small arm before and after optimization

It can be seen from Figure.4 that the maximum stress before and after the optimization of the boom appears at the position of the connecting part of the bearing hole and the connecting plate, where the fillet is not added, resulting in the stress concentration after loading, but the total stress is still within the yield strength of the material, and the maximum stress before optimization is 0.44766 MPa, and the maximum stress after optimization is 0.44693 MPa, its static strength is still within the yield strength of the material.

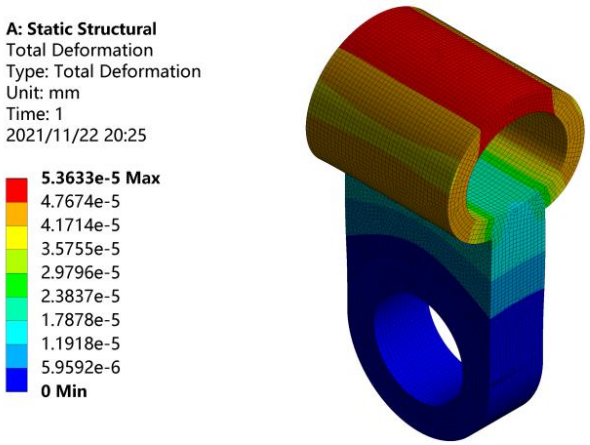

(a) Before

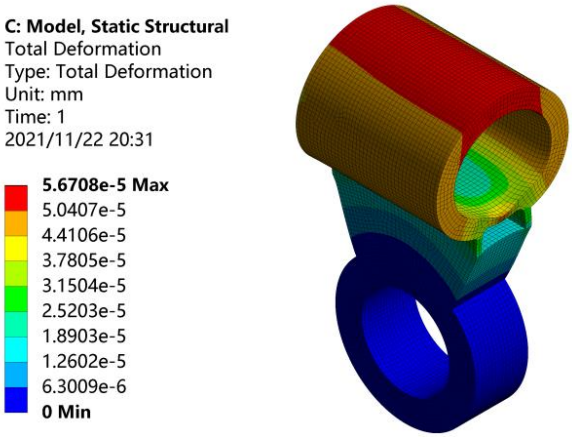

(b) After

Figure 5 Displacement Diagram of total deformation of small arm before and after optimization

From Figure.5, it can be seen that the maximum deformation displacement is 5.3635e-5mm before optimization and 5.6708e-5mm after optimization, there is little difference in displacement and deformation before and after optimization. According to the simulation data, the arm has the same resistance to deformation before and after optimization, and the optimized quality is 55.477% of the original quality, and the optimized quality is greatly reduced.The specific data changes before and after optimization are shown in Table 2.

Table 2 Changes of mechanical properties of small arm before and after optimization.

Optimization process	Mass (Kg)	Maximum total deformation (mm)	Maximum stress (MPa)
Before	2.7467	5.3635e-5	0.44766
After	1.5238	5.6708e-5	0.44693

2.2 Topology optimization of big arms

The big arm mainly controls the change of the

horizontal displacement of the manipulator before and after, when the topology of the big arm is optimized. The optimization model uses the most original structure quality is big, the optimization space is very big, therefore sets the quality to retain the original quality 30% , regarding optimizes before and after big arm's structure design as shown in Figure 6.

As can be seen from Figure.6, the optimized position is the connecting rod of two bearing holes and a part of bearing holes. The optimized density unit is reasonable. The overall volume is reduced from 7.6992e+5 mm3 to 3.8166e+5 mm3. The optimized volume is 49.57% of the original volume, the original mass was optimized from 6.0439 Kg to 2.996 Kg, and the optimized volume was 49.57% of the original volume.

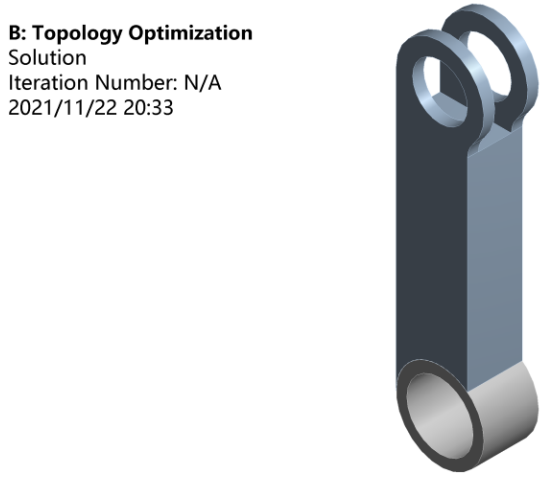

(a) Before

(b) After

Figure 6 Model comparison before and after big arm optimization

Similarly, the optimized arm model is simplified to meet the requirements of post-processing and the original density distribution. The simplified arm model is shown in Figure.7.

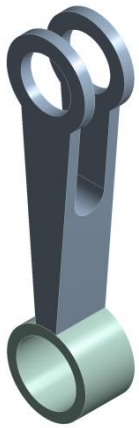

Figure 7 Simplified model of big arm after optimization

The static analysis of the simplified model before and after optimization is carried out under the same conditions. The applied bearing load is 200 N. The results of the static analysis are as follows.

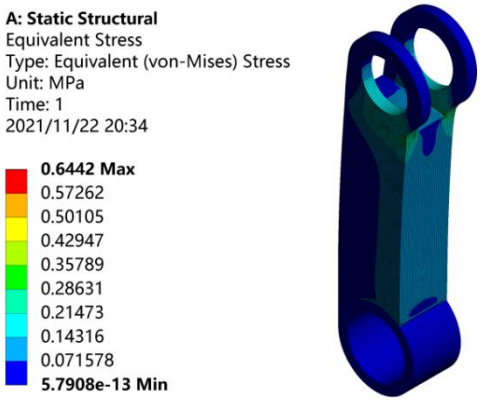

(a) Before

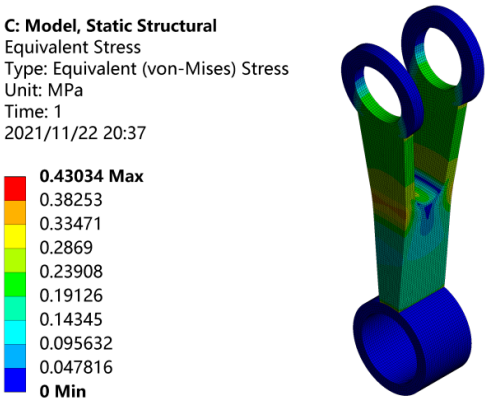

(b) After

Figure 8 Equivalent stress Nephogram of big arm before and after optimization

As can be seen from Figure.8, the stress concentration area of the arm is between the bearing hole and the connecting Rod. The maximum stress before optimization is 0.6442 MPa, and the maximum stress after optimization is 0.43034 MPa. The stress of the optimized model is less

than that before optimization, the static strength of the optimized model is better than that of the pre-optimized model, and it is all within the yield strength of the material.

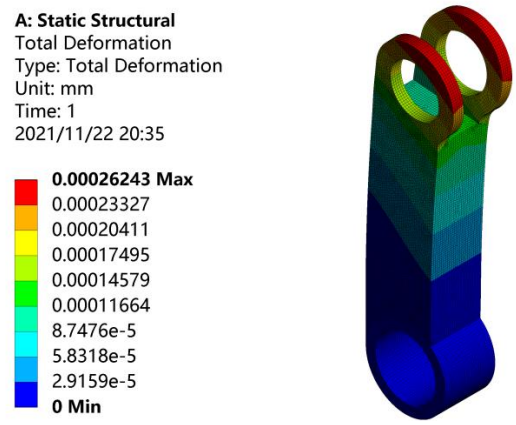

(a) Before

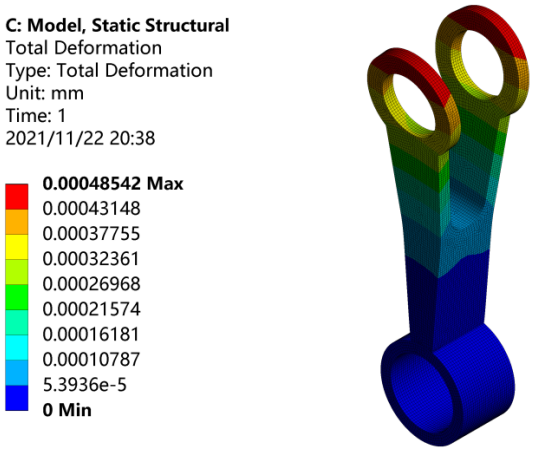

(b) After

Figure 9 Total deformation displacement diagram before and after big arm optimization

As can be seen from Figure.9, the maximum deformation displacement is 0.00026243 mm before optimization and 0.00048542 mm after optimization. The amount of deformation after optimization is slightly higher than the amount before optimization, but here according to our actual needs is to design this part as light as possible, so the quality of the parts to be greatly optimized, although the deformation resistance decreases slightly, the maximum deformation is still within the acceptable range, the stress decreases and the density distribution of the structure is reasonable, so the topological optimization results are also acceptable, the structure design achieves the expected ideal.

Table 3 Comparison of mechanical properties of big arms before and after optimization.

Optimization process	Mass (Kg)	Maximum total deformation (mm)	Maximum stress (MPa)
Before	6.0439	0.00026243	0.6442
After	2.996	0.00048542	0.43034

2.3 Topology optimization of rotating base

The rotating base part mainly controls the movement of the XY axis of the manipulator, and sets the quality restriction to 50% of the original mass according to the actual demand.Before and after the model is optimized for the rotating base, as shown in Fig.10.

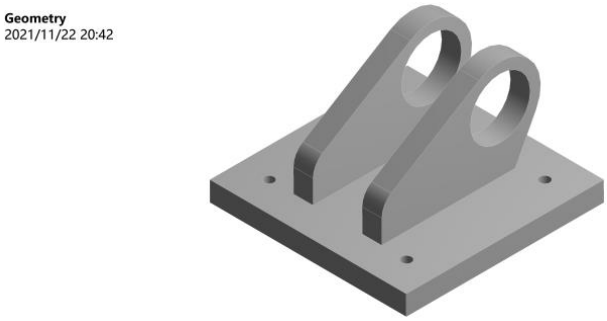

(a) Before

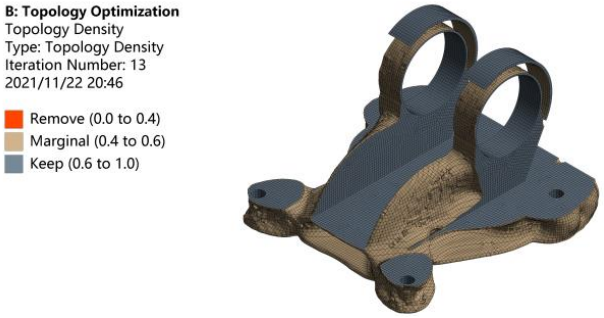

(b) After

Figure 10 Model comparison before and after optimization of rotating base

As can be seen from Figure. 10, the optimized density unit is mainly located at the base support plate. The overall volume of the structure decreased from 1.1439e+6mm3 to 6.1887e+5mm3, the overall volume decreased to 54.1% of the original volume, the overall mass decreased from 8.9798Kg to 4.8582Kg, and the overall mass decreased to 54.1% of the original volume, the simplified model reconstructed is shown in Figure11.

Figure 11 Simplified model after optimization of rotating base

Static analysis was carried out on the preoptimized and post-optimized simplified models under the same

conditions. The applied bearing load was 200N. The results of static analysis are shown in Figure12.

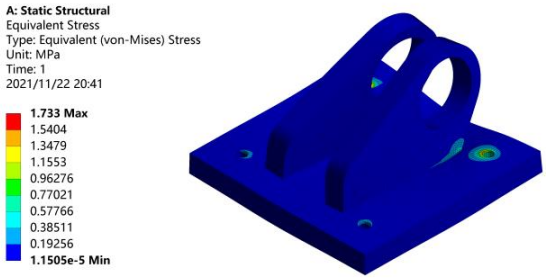

(a) Before

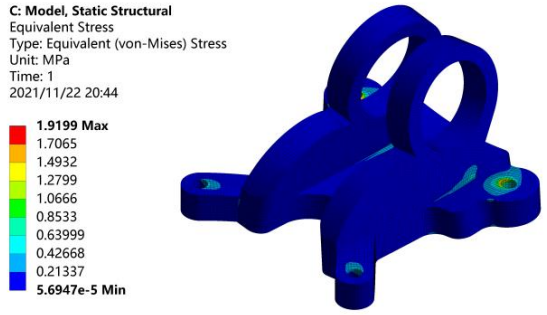

(b) After

Figure 12 Equivalent stress nephogram before and after optimization of rotating base

As can be seen from Figure12, the maximum stress is at the bolt hole, where the stress is concentrated. The maximum static stress of the structure is 1.733 MPa before optimization and 1.9199 MPa after optimization, and the stress rises slightly after optimization, but the change range is only 10.7% , which is still within the compressive strength of the material.

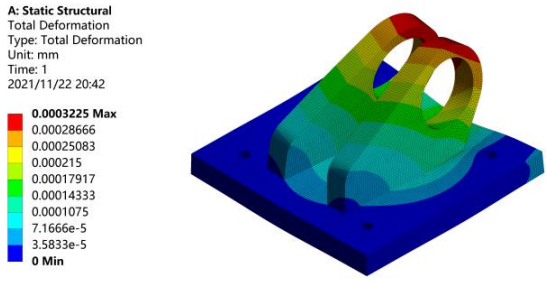

(a) Before

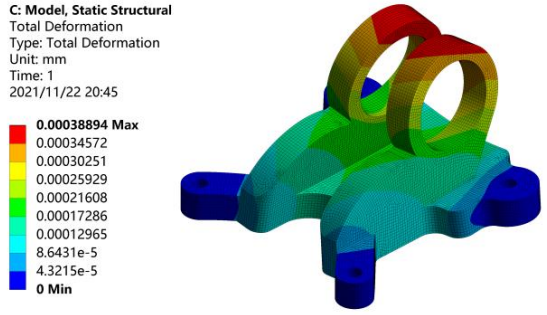

(b) After

Figure 13 Displacement Diagram of total deformation before and after optimization of rotating base

As can be seen from Figure13, the maximum deformation is 0.0003225mm before the whole structure is optimized and 0.00038894mm after the whole structure is optimized, it can be regarded as the same anti-deformation ability before and after optimization, and its structure design achieves the expected ideal.

A summary of the data before and after the rotation base optimization is shown in Table 4.

Table 4 Comparison of mechanical properties of rotating base before and after optimization.

Optimization process	Mass (Kg)	Maximum total deformation (mm)	Maximum stress (MPa)
Before	8.9798	0.0003225	1.733
After	4.8582	0.00038894	1.9199

3 Conclusion

The results of static analysis before and after optimization show that the mass of the manipulator is 17.7704 Kg before optimization and 9.378 Kg after optimization, and the total mass is reduced by 47.23%, the optimized model structure is more concise, the whole structure is more flexible when working, and the optimal effect is remarkable. Without changing the original mechanical properties, only the material distribution in the design area is changed, which shows that it is effective to apply the topology optimization method of variable density method to the 6-DOF manipulator, and the effect is remarkable. Through the application of this theory, the mass of the structure is reduced effectively and the lightweight design of the manipulator is achieved. At the same time, the optimized model is simplified by post-processing, which also makes the optimized model meet the requirements of manufacturability and machinability, and plays a reference role for the follow-up structure optimization of 6-DOF manipulator.

Conflict of Interest

The authors declares that there is no conflict of interest regarding the publication of this paper.

Acknowledgments

This work was supported in part by China intelligent robot project of firm-universities cooperative R&D under Grant No.2021JQR021, the Anhui Provincial Teaching Demonstration Course Project under Grant No.2020SJJXSFK0330, the demonstration experiment training center project of Anhui Polytechnic University under Grant No.2020sysx02, the Overseas Visiting and Research Project for Outstanding Young Backbone Talents in Universities of Anhui Province under Grant No.gxgwfx2019041, the Innovation Project for Returned Overseas Students in Anhui Province under Grant

No.2020LCX013, Key Research and Development Projects of Anhui Province under Grant No.202004b11020006, Scientific Research Foundation of Anhui Polytechnic University under Grant No.2020YQQ010, Anhui Polytechnic University Research Initiation Fund for Introducing Talents under Grant No.2019YQQ004, Anhui Polytechnic University Research Project under Grant No. Xjky019201905, Industrial Collaborative Innovation Fund of Anhui Polytechnic University and Jiujiang District under Grant No.2021cyxtb9, Open Project of Anhui Provincial Engineering Laboratory on Information Fusion and Control of Intelligent Robot under Grant No.IFCIR2020001, and Open project of Key Laboratory of industrial equipment quality big data Ministry of industry and information technology under Grant No.2021-IEQBD-05.

References

[1] Daniel Y G,Juan C T, 2020. Topology optimization of thermal problems in a nonsmooth variational setting: closed-form optimality criteria. Computational Mechanics: Solids, Materials, Complex Fluids, Fluid-Structure-Interaction, Biological Systems, Micromechanics, Multiscale Mechanics, Additive Manufacturing, 66(2),259-286.

[2] Vrionis P Y,Samouchos K D, 2021. Topology optimization in fluid mechanics using continuous adjoint and the cut-cell method. Computers and Mathematics with Applications(97):286-297.

[3] Noguchi Yuki, Yamada Takayuki, 2021. Level set-based topology optimization for graded acoustic metasurfaces using two-scale homogenization. Finite Elements in Analysis & Design, (1):196.

[4] Seebacher Philipp, Kaltenbacher Manfred, 2021. A pseudo density topology optimization approach in nonlinear electromagnetism applied to a 3D actuator. International Journal of Applied Electromagnetics and Mechanics, 65(3):545-559.

[5] Yuki Sato, Kazuhiro Izui, 2020. Robust topology optimization of optical cloaks under uncertainties in wave number and angle of incident wave. International Journal for Numerical Methods in Engineering, 121(17):3926-3954.

[6] Behrou R, Lotfi Reza, 2021. Revisiting element removal for density-based structural topology optimization with reintroduction by Heaviside projection. Computer Methods in Applied Mechanics and Engineering, 380:113799.

[7] Y S Han, B Xu, 2021. An efficient 137-line MATLAB code for geometrically nonlinear topology optimization using bi-directional evolutionary structural optimization method. Structural and Multidisciplinary Optimization, 63(5):2571-2588.

[8] Kambampati Sandilya,Gray Justin S, 2021. Level set topology optimization of load carrying battery packs. International Journal of Heat and Mass Transfer, (1):177.

[9] Seebacher Philipp, Kaltenbacher Manfred, 2021. A pseudo density topology optimization approach in nonlinear electromagnetism applied to a 3D actuator. International Journal of Applied Electromagnetics and Mechanics, 65(3):545-559.

[10] Yunfei Fu, Rolfe Bernard, 2020. SEMDOT: Smooth-edged material distribution for optimizing topology algorithm. Advances in Engineering Software, 150:1029.

Viser Technology Pte. Ltd.
Mechanical Engineering Science
DOI: 10.33142/mes.v4i1.7514

Research Article Open Access

Analysis of vibration attenuation characteristics of large thickness carbon fiber composite laminates

Yi-Qi WANG*, Chaoqun WANG, Pengxiao YANG, Ziao WANG, Tete CAO

Key Laboratory for Precision and Non-traditional Machining Technology of Ministry of Education, Dalian University of Technology, Dalian 116024, China

***Corresponding Author:** Yi-Qi WANG, E-mail address: wangyiqi@dlut.edu.cn*

Abstract:
The vibration attenuation and damping characteristics of carbon fiber reinforced composite laminates with different thicknesses were investigated by hammering experiments under free boundary constraints in different directions. The dynamic signal testing and analysis system is applied to collect and analyze the vibration signals of the composite specimens, and combine the self-spectrum analysis and logarithmic decay method to identify the fundamental frequencies of different specimens and calculate the damping ratios of different directions of the specimens. The results showed that the overall stiffness of the specimen increased with the increase of the specimen thickness, and when the thickness of the sample increases from 24mm to 32mm, the fundamental frequency increases by 35.1%, the vibration showed the same vibration attenuation and energy dissipation characteristics in the 0° and 90° directions of the specimen, compared with the specimen in the 45° direction, which was less likely to be excited and had poorer vibration attenuation ability, while the upper and lower surfaces of the same specimen showed slightly different attenuation characteristics to the vibration, the maximum difference of damping capacity between top and bottom surfaces of CFRP plates is about 70%.
***Keywords:** Carbon fiber composite laminates; Logarithmic decay method; Damping ratio; Natural frequency*

Introduction

Carbon fiber reinforced polymer (CFRP) have been widely used in aerospace, automotive and defense industries [3-6] due to their high specific strength and specific stiffness [1-2]. Due to the unique weight reduction advantages of carbon fiber composites, the application of large thickness CFRP is also becoming more and more common, such as a series of Airbus aircraft with large thickness CFRP joints and central wing boxes. In addition to meeting various mechanical properties, the vibration damping properties of CFRP are also very important, which affect the performance, safety and reliability of parts and systems [7]. As the most widely used marine propulsion device, the noise and vibration generated by ship propeller cannot be ignored. At present, there have been a lot of research on composite propellers to eliminate violent vibration [8-9].

Damping can be defined as the energy dissipation of a structure that generates vibrations [10-12]. The damping mechanism attenuates the vibration by converting the energy generated by the vibration into other forms of energy. While CFRP belongs to fiber reinforced resin matrix composites, its damping properties are significantly anisotropic as well as mechanical properties.

Gibson [13] and Zou [14] have made great contributions to the analysis of vibration testing methods by investigating modal testing techniques, including frequency response methods and time domain analysis as well as frequency domain analysis, to further analyze and study the response of structures subjected to excitation. In terms of experimental tests, Adams [15-16] and others used free beam bending vibration experiments to study the dynamic properties and damping of unidirectional composites at different temperatures. Pei and Li [17] used hammering experimental methods to study the effect of fiber orientation on the modal and damping ratios of unidirectional carbon fiber composite laminates. Riccardo [18] investigated the modal damping parameters of composite laminates by an experimental method of point-by-point excitation single-point test. Rueppel [19] and others applied logarithmic decay method and DMA analysis to analyze and study the damping properties of CFRP laminates and obtained the relationship between lay-up angle and damping properties. Pereira [20-21] used a combination of numerical calculations and experiments to preliminarily verify that variable angle lay-up can one

Copyright © 2022 by author(s) and Viser Technology Pte. Ltd. This is an Open Access article distributed under the terms of the Creative Commons Attribution-NonCommercial 4.0 International License (http://creativecommons.org/licenses/by-nc/4.0/), permitting all non-commercial use, distribution, and reproduction in any medium, provided the original work is properly cited.
Received on April 16, 2022; Accepted on May 11, 2022

adjust the laminate frequency and damping, and further investigated the multi-objective optimization to improve the fundamental modal frequency and the corresponding specific damping capacity of the laminate. In the study of the damping energy dissipation mechanism of CFRP, Tang [22] reviewed the damping mechanism of fiber-reinforced resin matrix composites. It can be seen that the research on CFRP materials is mainly focused on the overall damping characteristics in depth, while the research on the attenuation law and damping characteristics of vibration in different directions within CFRP laminates is very little at present.

This paper focuses on the damping characteristics in different directions on a large thickness CFRP laminate. Hammering experiments are used to analyze the attenuation of vibrations within large thickness CFRP laminates (the thickness is greater than 3mm) of different thicknesses in different directions on the upper and lower surfaces by means of frequency and time domains.

1 Experimental preparation

1.1 CFRP Specimen preparation

Two specimens were prepared by Resin transfer molding (RTM) process using T300 grade 0° /90° plain weave carbon fiber woven fabric. And E-51 resin is selected, which is produced by Wuxi Qianguang Chemical Materials Co. LTD. Different layers of the woven fabric were applied and the final CFRP specimens with thicknesses of 24 mm and 32 mm were obtained.

1.2 Experimental methods and apparatus

The hammer pulse method is based on frequency response functions and is widely used to describe the dynamic properties of vibrating systems [23].

The vibration test system is shown in Figure 1. The specimen is suspended on the experimental stand by a rubber elastic rope with certain stiffness to ensure free boundary conditions. The acceleration sensor is fixed at the measurement point with 502 binder and the output signal is sent to the data acquisition analyzer (INV3062-C1), and then the response signal is analyzed by the Coinv DASP V11 software.

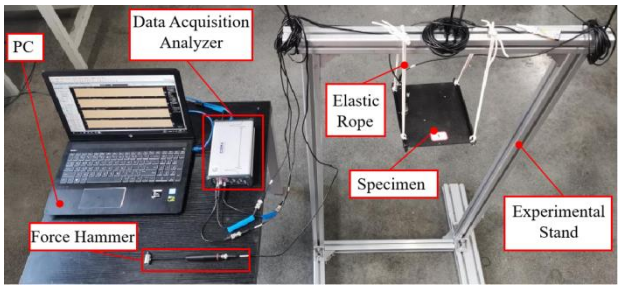

Figure 1 The vibration test system for CFRP laminate

The vibration sensor measurement point arrangement diagram is shown in Figure 2. The CFRP specimen was struck using an INV9310 impact force hammer to make the specimen vibrate freely and return to rest with damping, and six sets of experiments were conducted in six directions. Each experiment sensor was arranged at the center and end points of one of the 0°, 45° and 90° directions on the top surface (TS) and bottom surface (BS), respectively. Three taps were performed for each set of experiments, and the data were averaged to ensure the accuracy of the analysis.

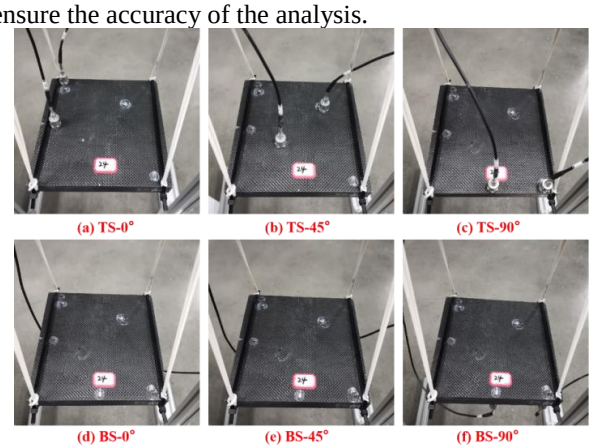

Figure 2 Arrangement of measurement points of acceleration sensors in different directions

(a) TS-0° (b) TS-45° (c) TS-90° (d) BS-0° (e) BS-45° (f) BS-90°

2 Results and discussion

2.1 Analysis of inherent frequency

The magnitude of the first natural frequency (i.e. fundamental frequency) of the laminate is a key indicator of the vibration characteristics of the structure. The acceleration output signal collected by the collector is processed by the software as a spectrogram, and the spectrogram is used to identify the first-order intrinsic frequency. The spectrum analysis of the collected data was carried out by Fast Fourier Transform (FFT).

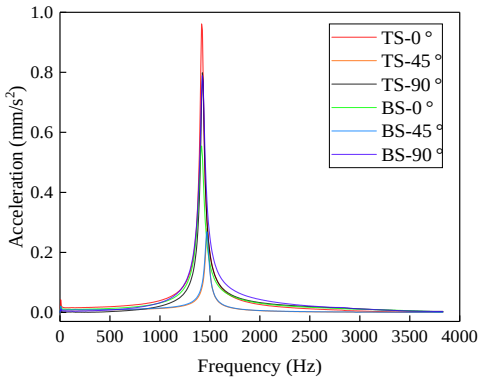

Figure 3 Spectra of the end points of the specimen with thickness of 24mm in each direction

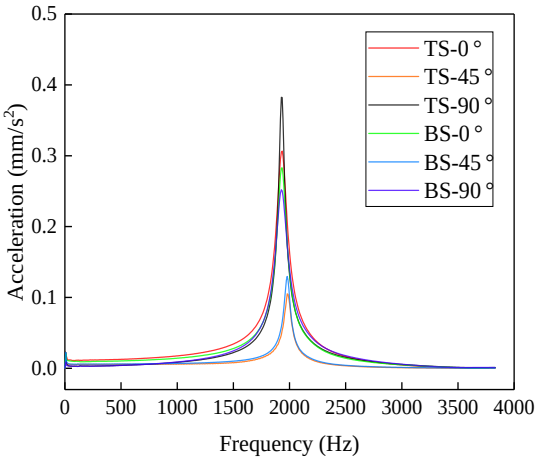

Figure 4 Spectra of the end points of the specimen with thickness of 32mm in each direction

The comparative analysis of Figure 3 and Figure 4 shows that the two specimens exhibit the same vibration law in the 0° and 90° directions on the upper and lower surfaces, and the same intrinsic frequencies can be calculated in these four directions. While in the 45° direction of the upper and lower surfaces showed a slight difference. Through the self-spectrum analysis of the specimen in 0° and 90° directions, it can be seen that the first-order inherent frequencies of the specimens with thicknesses of 24 mm and 32 mm are 1425.0 Hz and 1925.7 Hz, respectively. With the increase of the specimen thickness, the fundamental frequency of the specimen increases, which is closely related to the overall stiffness of the plate, and the specimens with better stiffness are less likely to resonate. While, the 45° directional curves of the two specimens with thicknesses of 24 mm and 32 mm calculated a slight increase in the intrinsic frequency with a boost of 3.16% and 2.59%. This shows that the transmission of vibration in the 45° direction is different from the 0° and 90° directions. Since the experimentally used CFRP is an anisotropic material with different strength and stiffness in either internal direction other than the fiber direction, and the stiffness in the 45° direction is increased relative to the fiber direction, the slightly higher fundamental frequency analysis results are identified and calculated.

2.2 Analysis of Logarithmic decrement

In the time domain waveform analysis, as shown in Figure 5 and Figure 6, the acceleration waveforms at the end points in each direction decay exponentially. Therefore, the free vibration decay method is the most intuitive and simple method to represent the vibration decay and damping performance of the end points in each direction.

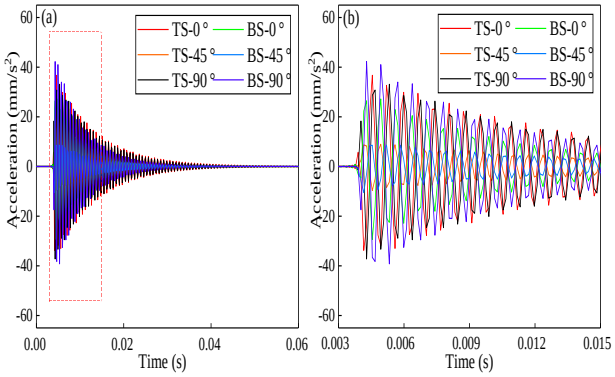

Figure 5 Time domain waveforms at the end points in each direction for a 24 mm thick specimen: (a) Full time domain diagram, (b) Time domain diagram of the start-up phase

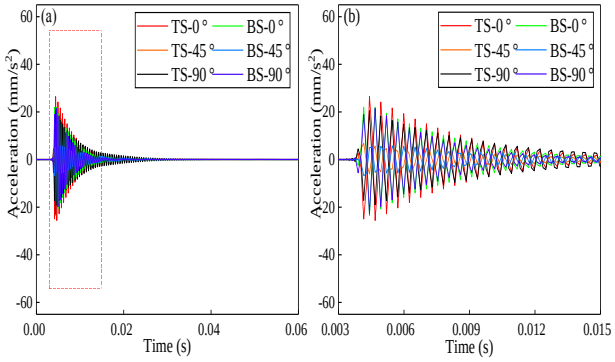

Figure 6 Time domain waveforms at the end points in each direction for a 32 mm thick specimen: (a) Full time domain diagram, (b) Time domain diagram of the start-up phase

Logarithmic decrement (δ) is commonly used as a parameter to characterize the damping properties of a material and is calculated as

$$\delta = \frac{1}{m} \ln \frac{A_n}{A_{n+m}} \quad (1)$$

where A_n and A_{n+m} are the nth and (n+m) th amplitudes on the decay curve, respectively.

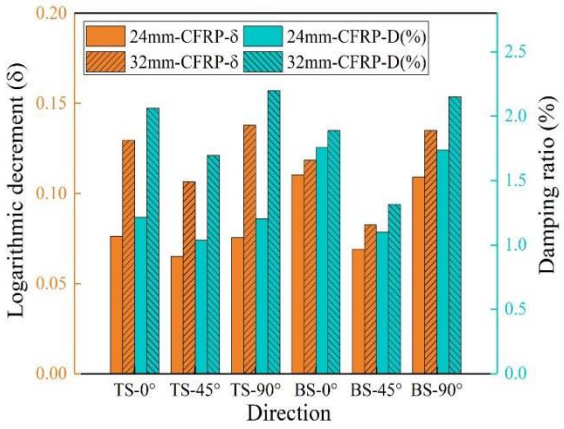

Figure 7 Logarithmic decrement and damping ratio of each direction of the two specimens

As can be seen in Figure 7, the specimen with a thickness of 32 mm has a higher logarithmic attenuation rate than the 24 mm specimen in all six directions measured, i.e., the 32 mm thickness specimen has a better attenuation effect on the vibration in these directions. In addition, when combined with Figure 5 and Figure 6, the two specimens were subjected to the same excitation force to generate vibration, the 32 mm CFRP plate recovered its initial stationary state in a shorter time. Moreover, combined with the time-domain waveforms, it can also be seen that the 45° direction has significantly lower vibration acceleration amplitude than the 0° and 90° directions at the onset of vibration. The reason for this is that CFRP has higher stiffness in the non-fiber direction of 45° , and has lower sensitivity and higher stability to shock and vibration. 32mm specimens show less susceptibility to excitation and more rapid abatement.

There are certain patterns and differences in the logarithmic attenuation rates in different directions of the same specimen. Compared with the 45° direction on both surfaces, the vibration attenuation ability is better in the 0° and 90° directions. 24mm specimens have better vibration attenuation ability in the 45° direction on the lower surface, while 32mm shows the opposite pattern.

2.3 Analysis of damping ratio

The damping ratio makes a dimensionless measure relative to the amplitude decay rate and represents the form of decay of the vibration of the specimen after being excited. The relationship between the logarithmic decay rate and the damping ratio is shown in Equation 2.

$$\delta = \frac{2\pi\zeta}{\sqrt{1-\zeta^2}} \approx 2\pi\zeta \tag{2}$$

Therefore, the damping ratio of each direction of the specimen can be calculated by Equation 3. The calculation results are also shown in Figure 7.

$$\zeta = \frac{\delta}{2\pi} \tag{3}$$

The trend of the damping ratio in each direction of the two specimens in Figure 7 shows that the 32mm CFRP specimen has better damping performance than the 24mm specimen, and this characteristic is especially shown in the specimen for vibration transmission in the in-plane. For example, the damping ratio in the 0° direction on the upper and lower surfaces is 69.78% higher than that of the 24 mm specimen, while the damping ratio in the 0° direction on the lower surface is only 7.40% higher than that of the 24 mm specimen.

For the same specimen, the vibration dissipation ability is very similar in the 0° and 90° directions, both directions are fiber directions, and the stiffness is the same in the in-plane. And the damping is lower than in the 45° direction for the upper and lower surfaces, which indicates that the vibration dissipation ability is relatively poorer in that direction. For the upper and lower surfaces, in the 0° and 90° directions, the energy dissipation ability of the lower surface is slightly higher or close to the same direction of the upper surface, which indicates that the damping performance of the thickness direction also plays a certain role when the vibration is transmitted to the lower surface under the same hammering force knocking situation, but its role is very limited, while in the 45° direction, the damping ability of the upper and lower surfaces is not much different.

3 Conclusion

Single-point impulse hammering experiments were conducted on two CFRP specimens with different thicknesses. The time domain analysis and the self-spectral analysis curves calculated by FFT were obtained by arranging acceleration sensors at the center and end points of 0° , 45° and 90° directions on the upper and lower surfaces of the specimens to study the attenuation and damping characteristics of the vibration in different directions on the two surfaces.

(1) The increase in thickness increases the overall stiffness of the CFRP laminate. The specimen with a thickness of 32 mm has a significant increase in the first natural frequency compared to the specimen with a thickness of 24 mm, and is also less likely to be excited.

(2) The results of the intrinsic frequencies of the specimens obtained by the self-spectral analysis curves differ in the 45° direction and other directions, and the calculated results in the 45° direction are slightly higher. Combined with the maximum amplitude of the end-point vibration in each direction on the time domain analysis curve, the 45° direction also shows a lower level. Both confirm that the CFRP plate has higher stiffness and insensitivity and stability to vibration and impact in the 45° direction on the upper and lower surfaces of the CFRP laminate.

(3) By comparing the results of logarithmic decrement and damping ratio at the end points of different directions, it can be found that the logarithmic decrement and damping ratio in the 45° direction are significantly lower than those in the other directions, which also indicates that this direction has higher stiffness and thus leads to worse damping performance in this direction, for the 0° and 90° directions (fiber direction) of the top and bottom surfaces of the specimen, the damping performance shows consistency.

Acknowledgments

This work was supported by the Fundamental Research Funds for the Central Universities [grant nos. DUT21LAB108, DUT22LAB401].

References

[1] Werken N, Tekinalp H, Khanbolouki P, et al, 2019. Additively Manufactured Carbon Fiber-Reinforced Composites: State

of the Art and Perspective. Additive Manufacturing, (31): 100962.
[2] Du X, Zhou H, Sun W, et al, 2017. Graphene/epoxy interleaves for delamination toughening and monitoring of crack damage in carbon fibre/epoxy composite laminates. Composites Science and Technology, (140): 123-133.
[3] Venkatachari A, Natarajan S, Haboussi M, et al, 2016. Environmental effects on the free vibration of curvilinear fibre composite laminates with cutouts. Composites Part B, (88): 131-138.
[4] Subramani M, Ramamoorthy M, 2020. Vibration analysis of multiwalled carbon nanotube-reinforced composite shell: An experimental study. Polymers and Polymer Composites, 28(4): 223-232.
[5] Treviso A, Genechten BV, Mundo D, et al, 2015. Damping in composite materials: Properties and models. Composites Part B: Engineering, (78): 144-152.
[6] Yan L, Sc A, Xh A, 2017. Multi-scaled enhancement of damping property for carbon fiber reinforced composites. Composites Science and Technology, (143):89-97.
[7] Zhang J, Yang H, Chen G, 2019. Damping of carbon fibre-reinforced plastics plates with holes. Plastics, Rubber and Composites, 48(10): 432-439.
[8] Mao Y, Young Y L, 2016. Influence of skew on the added mass and damping characteristics of marine propellers. Ocean Engineering, 121: 437-452.
[9] Mulcahy N L, Prusty B G, Gardiner C P, 2010. Hydroelastic tailoring of flexible composite propellers. Ships and Offshore structures, 5(4): 359-370.
[10] Abramovich H, Govich D, Grunwald A, 2015. Damping measurements of laminated composite materials and aluminum using the hysteresis loop method. Progress in Aerospace Sciences, (78): 8-18.
[11] Assarar M, Zouari W, Ayad R, et al, 2018. Improving the damping properties of carbon fibre reinforced composites by interleaving flax and viscoelastic layers. Composites Part B: Engineering, (152): 248-255.
[12] Lin H, Xiang Y, Yang Y, 2016. Coupled vibration analysis of CFRP cable-tube system under parametric excitation in submerged floating tunnel. Procedia engineering, (166): 45-52.
[13] Gibson R F, 2000. Modal vibration response measurements for characterization of composite materials and structures. Composites Science and Technology, 60(15): 2769-2780.
[14] Zou Y, Tong L, Steven G P, 2000. Vibration-based model-dependent damage (delamination) identification and health monitoring for composite structures - a review. Journal of Sound and vibration, 230(2): 357-378.
[15] Adams R D, Maheri M R, 2003. Damping in advanced polymer-matrix composites. Journal of Alloys & Compounds, 355(1-2): 126-130.
[16] Maheri M R, Adams R D, 2003. Modal vibration damping of anisotropic FRP laminates using the Rayleigh–Ritz energy minimization scheme. Journal of sound and vibration, 259(1): 17-29.
[17] Pei X Y, Li J L, 2012. The effects of fiber orientation on the vibration modal behavior of carbon fiber plain woven fabric/epoxy resin composites. Advanced Materials Research. Trans Tech Publications Ltd, 391: 345-348.
[18] Vescovini R, Bisagni C, 2015. A procedure for the evaluation of damping effects in composite laminated structures. Progress in Aerospace Sciences, 78: 19-29.
[19] Rueppel M, Rion J, Dransfeld C, et al, 2017. Damping of carbon fibre and flax fibre angle-ply composite laminates. Composites Science & Technology, 146: 1-9.
[20] Pereira D A, Guimarães TAM, Resende H B, et al, 2020. Numerical and experimental analyses of modal frequency and damping in tow-steered CFRP laminates. Composite Structures, 244: 112190.
[21] Pereira D A, Sales T P, Rade D A, 2021. Multi-objective frequency and damping optimization of tow-steered composite laminates. Composite Structures, 256: 112932.
[22] Tang X, Yan X, 2020. A review on the damping properties of fiber reinforced polymer composites. Journal of Industrial Textiles, 49(6): 693-721.
[23] Ding G, Xie C, Zhang J, et al, 2016. Modal analysis based on finite element method and experimental validation on carbon fibre composite drive shaft considering steel joints. Materials Research Innovations, 19(sup5): 748-753.

Viser Technology Pte. Ltd.
Mechanical Engineering Science
DOI: 10.33142/mes.v4i1.7515

Research Article Open Access

Design and motion control analysis of double helix wall climbing robot

Jinzhan WANG[1], Minglu CHI[1*], Yue MA[2], Qinchao REN[3], Mengqing HUANG[1], Yibo CHEN[1], Ruihua REN[1], Jinyu WANG[1], Si LIU[1]

1 School of Intelligent Engineering, Henan Institute of Technology, Xinxiang, Henan45300, China
2 School of Civil Engineering, Harbin University, Harbin, 150086, China
3 Jiangsu Huibo Robot Technology Co. LTD, Jiangsu Suzhou 215121, China

***Corresponding Author:** Minglu CHI, School of Intelligent Engineering, Henan Institute of Technology, Xinxiang, Henan, China; cmlcml86@163.com*

Abstract:
For the detection environment of complex walls such as high-rise buildings, a double helix wall climbing robot (DHWCR) with strong adsorption force and good stability is designed and developed, which uses symmetrical propellers to provide adsorption force. The symmetrical driving structure can provide smooth thrust for the DHWCR, so that the robot can be absorbed to the wall surface with different roughness. A left and right control frame with multiple degrees of freedom is designed, which can adjust the fixed position of the brushless propeller motor in the front and back directions, realize the continuous adjustable thrust direction of the robot, and improve the flexibility of the robot movement. Using the front wheel steering mechanism with universal joint, the steering control of the DHWCR is realized by differential control. In the vertical to ground transition, the front and rear brushless motors can provide the pull up and oblique thrust, so that the DHWCR can smoothly transition to the vertical wall. The motion performance and adaptability of the DHWCR in the horizontal ground and vertical wall environment are tested. The results show that the DHWCR can switch motion between the horizontal ground and vertical wall, and can stably adsorb on the vertical wall with flexible attitude control. The DHWCR can move at a fast speed. The speed on the horizontal ground is higher than that on the vertical wall, which verifies the feasibility and reliability of the DHWCR moving stably on the vertical wall.

***Keywords:** Double helix; Wall climbing robot; Reverse thrust adsorption; Structural design; Motion control*

Introduction

Recently, skyscrapers have become an indispensable part of modern cities. While high-rise buildings bring benefits to people, they also bring many problems, such as the cleaning, quality monitoring and maintenance of the exterior wall of high-rise buildings. Wall climbing robots (WCRs) can replace human beings to complete many extreme tasks [1-2]. By integrating ground mobile robots with climbing adsorption technology, they can efficiently operate in vertical altitude [3-4]. The research area of WCRs has steadily gained interest over the years as a promising approach to remote inspection and maintenance of big and hard to reach spaces. At present, WCRs are mainly applied in industries, railways, oil tanks, shipping, fire departments and reconnaissance activities, and can replace human beings to perform building deconsolization, glass exterior wall cleaning, aerial circuit maintenance, anti-terrorism reconnaissance and hull detection [5-8].

Many different approaches have been proposed for the WCRs' adhesion including magnetic, pneumatic, mechanical and material-based methods, and their locomotion including leg and wheel-based, sliding frames and sequential robotic structures. According to the adsorption method, the WCR can be divided into magnetic adsorption, bionic, vacuum adsorption, and reverse thrust [9-12]. According to the movement mode, it can be divided into wheel, crawler, foot, and wheel-foot compound movement.

The magnetic adsorption WCR can be applied only in the ferrous medium of the structure. This kind of robot can be further subdivided into two adsorption forms, namely permanent magnet adsorption and electromagnetic adsorption, both of which have their own advantages. At present, permanent magnet adsorption is more widely used [13-14]. Magnetic adsorption WCR through magnetic material adsorption to the wall surface, complete the wall cleaning task. However, it is only applicable to the wall surface of magnetic materials with poor adaptability, so it is mainly used to detect the inner

Copyright © 2022 by author(s) and Viser Technology Pte. Ltd. This is an Open Access article distributed under the terms of the Creative Commons Attribution-NonCommercial 4.0 International License (http://creativecommons.org/licenses/by-nc/4.0/), permitting all non-commercial use, distribution, and reproduction in any medium, provided the original work is properly cited.
Received on April 4, 2022; Accepted on May 23, 2022

and outer surfaces of large metal buildings. Magnetic adhesion methods can be applied only in the ferrous medium of the structure; however, pneumatic adhesion methods are well suited in WCRs for glass curtain wall and other structures.

Bionic robots are WCRs that imitate the characteristics of animal feet or pastes. This kind of bionic robot using adhesive material has the characteristics of complex drive control and fuzzy hook, so its application scope is relatively narrow. The robot is highly adaptable to the wall surface, but the cost is high. According to different adsorption methods, it can be divided into dry adhesion and wet adhesion [15-17]. However, at present, the technology of bionic WCR is immature, and the load capacity of robot is not strong. The vacuum adsorption WCR is the earliest robot, which is divided into active vacuum and passive vacuum. The active vacuum depends on the vacuum generator/pump and other accessories, and the passive vacuum is created by pressing the suction cups without using any electric power [18].

It is seen from these developed adsorption methods that reverse thrust is the most used and suitable technique for developing WCRs. RTAWCR is a kind of robot that uses screw pumps or ducted fans to generate appropriate thrust to achieve wall adsorption [19]. This force is relatively stable, and the robot can be reliably adsorbed on the wall. Since the generating device does not touch the wall, the robot does not have high requirements for the roughness of the wall. The thrust can be controlled simply by the switch of the wings. Desorption can be achieved when the power supply stops.

By comprehensive analysis of the above types of WCRs, it can be seen that although existing WCRs have wall-climbing functions, they generally have problems such as unstable adsorption, low stability, poor obstacle climbing ability, great potential safety hazards and low walking efficiency. And part of the bionic foot is expensive, there are restrictions on all aspects of the wall requirements.

To solve the above problems, this paper designs a double helix wall-climbing robot (DHWCR) with strong adsorption force and good stability, which can move on the horizontal ground and vertical wall. The propeller head and the front wheel steering mechanism can make the DHWCR flexibly switch between the horizontal ground and the corner surface. The DHWCR can climb up, down and turn on the 90 ° wall, while exploring the surrounding environment. Under the condition that the DHWCR can absorb effectively, the multi-directional turning drive control is realized. The speed test experiments are carried out on the horizontal ground and the vertical wall. The results show that the DHWCR can switch freely between the horizontal ground and the vertical wall, and can stably adsorb on the vertical wall with stable attitude control. The moving speed on the horizontal ground is higher than that on the vertical wall. The flexible driving control has laid a foundation for the obstacle crossing, detection and inspection of the DHWCR when moving on the wall.

1 Overall design of DHWCR adsorption drive control

In order to make the DHWCR complete its work in various environments, it is necessary to ensure the overall stability of the robot as far as possible during the climbing process. The DHWCR should be as lightweight as possible, so that the robot can be more stable adsorption on the wall. The overall design of the DHWCR system includes two parts: hardware and software design. Figure 1 shows the overall control design scheme.

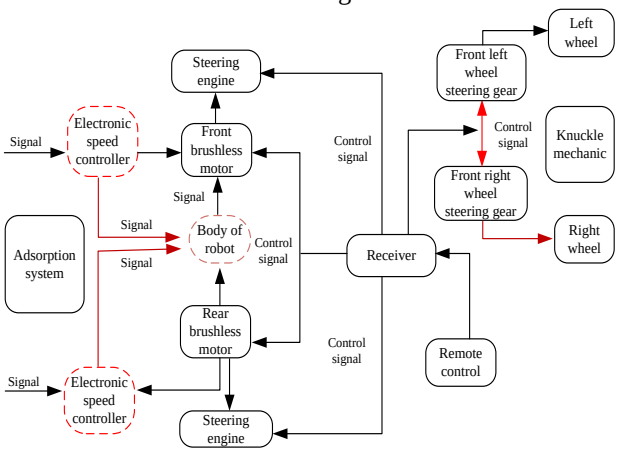

Figure 1 Overall control design of DHWCR

The overall structure of the DHWCR is shown in Figure 2, including the propeller head, brushless motor module, front wheel steering mechanism module, propeller steering gear control template and wireless handle control module. The motion control of the DHWCR and the brushless motor can be adjusted according to the steering gear. The DHWCR has low requirements on the wall, which can ensure the stable adsorption on the wall surface, and has a certain load capacity. At the same time, the reverse thrust can be adjusted by changing the motor control signal.

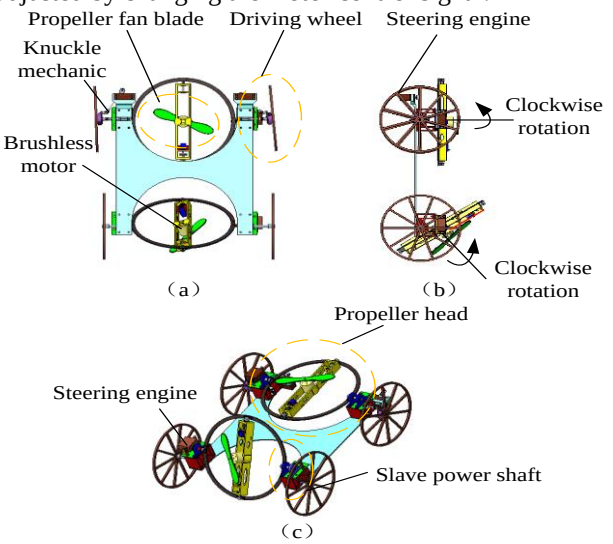

Figure 2 Three-dimensional diagram of the overall structure of a DHWCR

2 Structure design and motion control of DHWCR

2.1 Propeller head

In order to realize the stable adsorption motion of the DHWCR, the design of the head should be able to adjust the angle between the propeller and the climbing wall. As shown in Figure 3, the gimbal fixing device includes steering gear, brushless motor, bearing, power rod and outer ring. In the adsorption movement, the direction of the tension can be adjusted by controlling the steering gear through the controller. The head structure has multiple degrees of freedom and can adapt to different types of concave and convex wall adsorption. Due to the simultaneous operation of two brushless motors, the front and rear directions can be adjusted arbitrarily, which improves the climbing efficiency and the stability of adsorption.

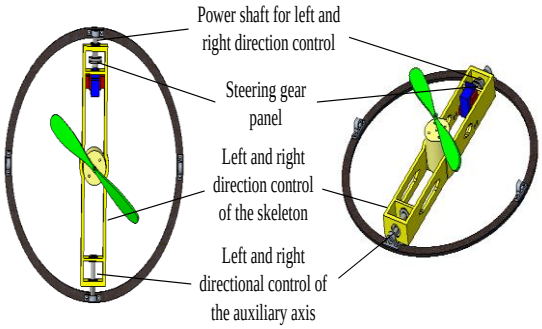

Figure 3 Design of propeller head

2.2 Front wheel steering mechanism

The steering mechanism module of the DHWCR includes universal joint, steering gear, connecting rod, etc. Signals can be sent to the Arduino control board through the controller to realize the control of the steering gear. Steering mechanism module has a steering gear on the left and right sides, through the connecting rod to drive the hub to achieve steering. The steering mechanism module is connected by multiple universal joints, which is light in weight and has high turning efficiency. It can realize fast turning on the horizontal and vertical walls and has high stability. Figure 4 shows the three-dimensional diagram of the front wheel steering mechanism module.

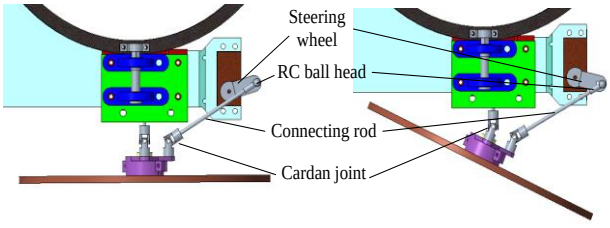

Figure 4 Front wheel steering mechanism module diagram

2.3 The linear motion of the DHWCR

The overall motion of the DHWCR can be divided into two parts: the straight motion on the wall and the straight motion on the ground. When moving in a straight line on the ground, the front and rear propellers form the same included angle with the ground, the brushless motor rotates at a high speed, and the air inside the paddle flows at different speeds from the air outside, generating a tension. Due to the different included angle with the ground, the tension finally pushes the DHWCR forward at different speeds, as shown in Figure 5.

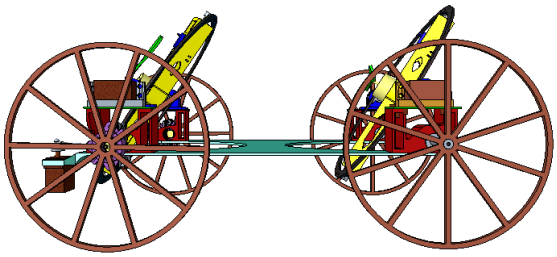

Figure 5 3D diagram of horizontal ground motion of DHWCR

When the DHWCR works on a vertical wall, it needs to overcome its own gravity, so in order to keep the robot crawling on the vertical plane, it needs to generate a slanting downward thrust, and in the direction of the reaction force with the wall, it will generate a tension opposite to gravity. The designed propeller head has multiple degrees of freedom, which can realize 180 ° rotation in four directions, as shown in Figure 6. The design of the double helix head can ensure that when the wall roughness and wall angle change, it can still adjust the speed and angle of the double brushless motor, adjust the tension, to ensure the stable movement of the DHWCR.

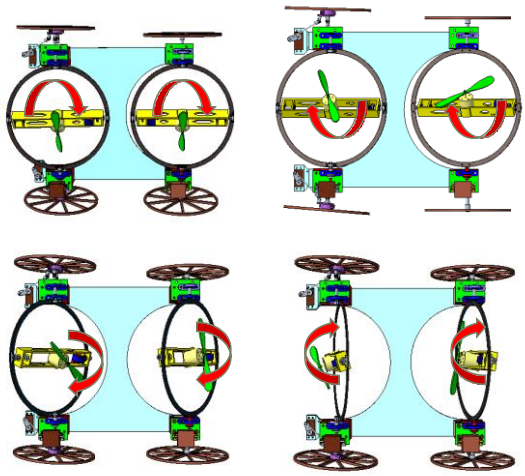

Figure 6 Schematic diagram of front, rear, left and right propeller head rotation

2.4 The steering motion of the DHWCR

In order to achieve smooth steering motion, the steering mechanism includes universal joint, steering gear,

connecting rod and chuck. The controller sends signals and transmits them to the steering gear for control. The DHWCR is installed with two steering gear. When the steering gear rotates to different positions, the hub angle connected by connecting rod also rotates accordingly, which can realize smooth steering from left to right. The left and right sides of the steering mechanism use six universal joints on each side, which is light in weight and high in turning efficiency. When moving on the plane and vertical walls, there will be no side component force. Figure 7 shows the turning diagram of the DHWCR.

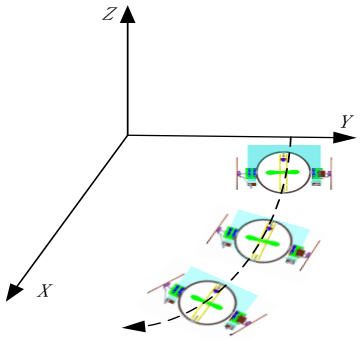

Figure 7 Steering diagram of the DHWCR

3 Structure design and motion control of DHWCR

3.1 The program design of propeller steering control module

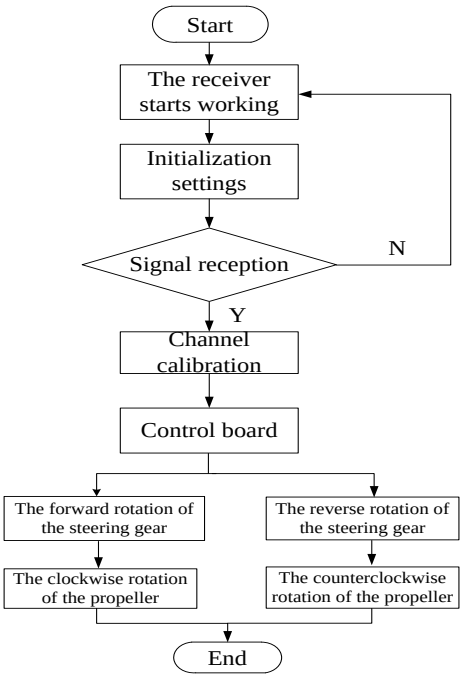

Figure 8 The flow chart of propeller steering machine control module program design

After receiving the signal through the receiver, the DHWCR controls the steering gear, and drives the bearing and brushless motor to control the rotation of the frame. When the brushless motor is working, it will produce downward tension in different directions. The receiver has a multi-channel control mode. The propeller steering machine is connected with different channels, which can realize the separate transmission of two signals. The direction of the fixed position of the front brushless motor and the direction of the fixed position of the rear brushless motor can be controlled respectively. The flow chart of propeller steering machine control module program design is shown in Figure 8.

3.2 Program design of front wheel steering mechanism module

After receiving the signal, the steering gear controlling the front wheel steering mechanism drives the connecting rod to make the hub turn around. Part of the control procedure is as follows.

```
SoftwareSerial softSerial(4, 2); //rxt    txt
char cmdChar = '5';
char cmdCharSave = cmdChar;
void setup() {
myservo1.attach(9);
   myservo2.attach(6);
   softSerial.begin(9600);
   delay(100);
   Serial.begin(9600);
   delay(100);
   myRadio.begin();
   myRadio.setChannel(115);
   myRadio.setPALevel(RF24_PA_MAX);
   myRadio.setDataRate( RF24_250KBPS );
myRadio.openReadingPipe(1,addresses[0]);
   myRadio.startListening();}
Servo myservo1;
Servo myservo2;
int i = 0;
void youzhuan()
{
 for (i = 0; i < 90; i++)
{
myservo1.write(i);
myservo2.write(i);
delay(10);
}
}
void zuozhuan()
{
for (i = 90; i >= 0; i--) { //  从 90 °到 0 °
myservo1.write(i);
myservo2.write(i);
   delay(10);
}
}
```

3.3 Program design of brushless motor module

The receiving controller can adjust the speed of the propeller brushless motor and transmit the control signal to the DHWCR. For different wall surface, the tension can be

adjusted, the front and rear brushless motor work at the same time. When moving from the horizontal ground to the vertical wall, the brushless motor generates upward tension. The brushless motor controls the frame to rotate to a certain angle, and pushes the DHWCR to realize the transition from plane to vertical. The software design flow chart of brushless motor module is shown in Figure 9.

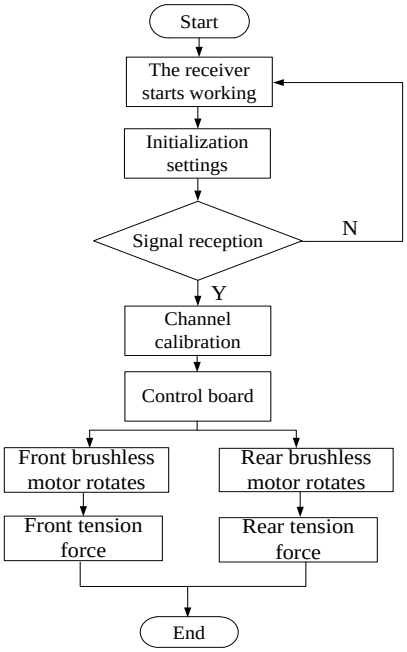

Figure 9 Brushless motor module software design flow chart

4 Adsorption motion test of DHWCR

4.1 Control board debugging

After entering the compilation environment, select the corresponding development board and port, compile and fire the program. When the indicator on the control board is off, open the port and observe the data displayed on the port, as shown in Figure 10.

```
sketch_may06c §
#define BLINKER_WIFI

#include <Blinker.h>
#include <Servo.h>
char auth[] = "80fa06f96a09";
char ssid[] = "HONOR 9X";
char pswd[] = "5211314r";
#define BUTTON_1 "btn-abc"

BlinkerButton Button1(BUTTON_1);
//新建组件
BlinkerSlider Slider1("A");
BlinkerSlider Slider2("B");
BlinkerSlider Slider3("C");
BlinkerSlider Slider4("D");
BlinkerSlider Slider5("E");
BlinkerSlider Slider6("F");
//声明舵机
Servo Aservo;
Servo Bservo;
Servo Cservo;
```

Figure 10 Arduino compilation environment

Before power-on, short connect the GPIO 0 and GND ports of the ESP32-CAM module. This will make the ESP32-CAM enter the download and start mode. Otherwise, the Arduino IDE will report an error. Fritzing simulation software is used to select ESP32-CAM module and USB-to-serial port download, and the circuit simulation connection as shown in Figure 11 is established.

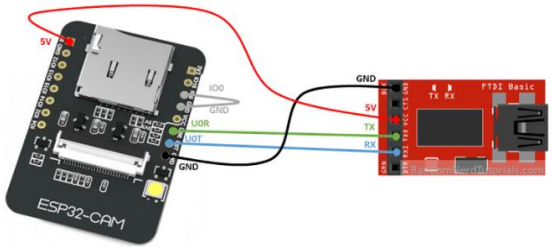

Figure 11 Program download Fritzing simulation wiring diagram

After the test code is burned, disconnect the GPIO 0 from GND, let the ESP32-CAM enter memory startup mode, and then power on the ESP32-CAM again. Open the serial port monitor of the software, select the transmission baud rate, and press the RST button. Open the software serial port. If all is well, the IP is printed on the serial port monitor and can be wirelessly controlled by connecting the Blinker, as shown in Figure 12.

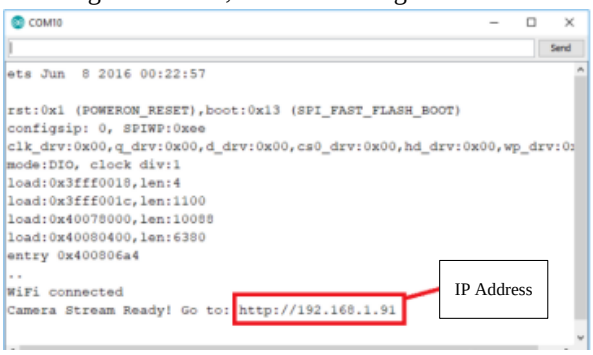

Figure 12 IP address of the serial port

4.2 The complete structure of the DHWCR

The whole machine of the DHWCR mainly includes propeller head, RC receiver, front wheel steering mechanism, propeller steering engine control module, 3D printed body and power supply, as shown in Figure 13. After the overall installation, switch on the power supply of the brushless motor, and test the pulling direction provided by the brushless motor of the front and rear wheels. If the brushless motor of the front and rear wheels provides upward pulling force when they work normally, the wiring is correct; On the contrary, the brushless motor needs to switch the two wires.

In normal operation, the front and rear propeller steering gear rotates 45 ° respectively, and the front and rear brushless motor generates a tension angle of 45 °with the direction of advance. The DHWCR obtains the forward power and the robot walks forward. The fixed propeller head will make the front and rear brushless

motors rotate with multiple degrees of freedom, providing different directions of tension angle. The tension generated by the front and rear brushless motors in different directions will generate an angle with the vertical wall, which can ensure that the DHWCR can complete the adsorption movement on the vertical wall.

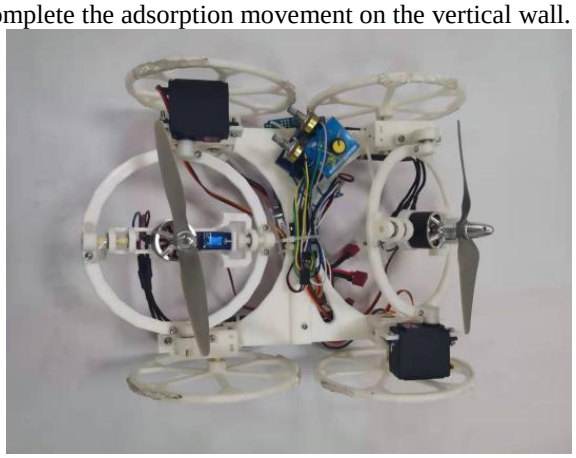

Figure 13 Complete structure of the DHWCR

4.3 Adsorption test of DHWCR

In order to verify the feasibility and stability of the DHWCR in the outer wall, the horizontal ground motion and the wall motion at different angles are tested. The speed of the DHWCR is measured, and the distance of 1m, 2m and 3m is set on the horizontal ground for testing. Each distance is tested three times, and the forward speed is measured by a timer.

Figure 14 The horizontal ground of the DHWCR moves in a straight line

Table 1 Horizontal ground velocity measurement of the DHWCR

Distance /m	No.	Time /s	Velocity m/s	Average velocity m/s
	1	2.69	0.372	
1	2	3.01	0.332	0.351
	3	2.87	0.348	
	1	3.68	0.543	
2	2	4.10	0.487	0.521
	3	3.75	0.533	
	1	4.96	0.605	
3	2	4.58	0.655	0.683
	3	3.80	0.789	

The inclined wall of 30°, 45°, 60° and 75° is designed for test verification. When the DHWCR moved from the ground to the wall at a small angle, under the action of the brushless motor tension, the robot would move directly from the ground to the inclined surface. Figure 15 shows the motion of the DHWCR on the inclined wall of 30°, 45°, 60°and 75°.

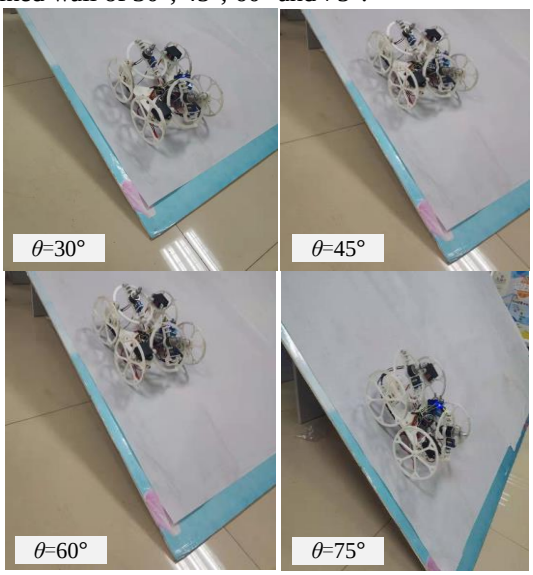

Figure 15 Movement of the inclined wall of 30°, 45°, 60° and 75°

A distance of 1 m and 2 m is set on the vertical wall, and the test is repeated three times for each. The measured velocities are shown in Table 2.

Table 2 Vertical wall velocity measurement of the DHWCR

Distance /m	No.	Time /s	Velocity m/s	Average velocity m/s
	1	14.75	0.068	
1	2	12.36	0.081	0.069
	3	17.09	0.058	
	1	27.53	0.072	
2	2	35.30	0.057	0.064
	3	30.58	0.065	

It can be obtained that the average speed at the horizontal ground distance of 1m, 2m and 3m is 0.351m/s, 0.521m/s and 0.683m/s respectively, and the average speed at the vertical wall crawling distance of 1m and 2m is 0.069m/s and 0.064m/s respectively.

5 Conclusion

In this paper, the hardware and software of the DHWCR are designed and tested for the important problems in the adsorption stability and attitude control. The main conclusions are as follows.

(1) A DHWCR with strong adsorption force and good stability is designed and developed, which is mainly

composed of propeller head, brushless motor module, front wheel steering mechanism module, propeller steering gear control template, wireless handle control module, etc. The left and right control frame with multiple degrees of freedom is designed, which can move on the horizontal ground and vertical wall.

(2) The propeller head and front wheel steering mechanism of the DHWCR can make the robot flexibly switch between the horizontal ground and the vertical wall. In order to ensure that the DHWCR can effectively adsorb, the multi-directional turning drive control is realized, and the movement flexibility is good. By changing the rotation position of the front and rear steering gear and changing the angle of the hub connected with the connecting rod, the DHWCR can achieve smooth steering from left to right and improve the turning efficiency.

(3) Speed test, small slope climbing test and 90 °wall stability adsorption test are carried out on the DHWCR on the horizontal ground and vertical wall. The results show that the DHWCR can switch freely between the horizontal ground and vertical wall, and can stably adsorb on the vertical wall with stable attitude control. The DHWCR moves faster on the horizontal ground than on the vertical wall, which also verifies the feasibility of the robot moving stably on the vertical wall.

The breakthrough of the driving control technology of the new DHWCR has laid a foundation for the nondestructive testing of high-rise buildings and the testing of complex vertical walls.

Conflict of Interest

Te author declare that there is no conflict of interest regarding the publication of this paper.

Acknowledgement

This work was supported by the Key Research Development and Promotion Special Project of Henan Province, under Grant 212102310119 and 212102210358, Scientific Research Foundation for High-level Talents of Henan Institute of Technology, under Grant KQ1869, 2021 Provincial Higher Education Teaching Reform General Project "Research and Practice of Grassroots Teaching Management Construction in Local Application-oriented Universities under the Background of Professional Certification", under Grant SJGY20210520, University-Industry Collaborative Education Program, under Grant 202101187010 and 202102120046, Innovation and Entrepreneurship Training Program for College Students of Henan Province, under Grant 202211329011, Educational and Teaching Reform Research and Practice Project of Henan Institute of Technology, under Grant 2021-YB023 and JJXY-2021005, Innovative Education Curriculum Construction Project of Henan Institute of Technology, under Grant CX-2021-005, 2022 Xinxiang Federation of Social Sciences Research topic, under Grant SKL-2022-254 and SKL-2022-228, 2022 Annual Research Topic of Henan Federation of Social Sciences, under Grant SKL-2022-2692, 2022 Annual Research Project of Henan Federation of Social Sciences: "Research on Rural Revitalization Strategy of Financial Service Model Innovation in Henan Province", under Grant SKL-2022-2692.

References

[1] R D Dethe, S B Jaju, 2014. Developments in wall climbing robots: a review, International Journal of Engineering Research and General Science, 2(3):33–42.

[2] W Siyuan, 2021. Research status and future development of wall-climbing robot, 2021 International Conference on Electronics, Circuits and Information Engineering (ECIE) :122–130.

[3] S T Nguyen, H M La, 2021. A climbing robot for steel bridge inspection, Journal of Intelligent & Robotic Systems, 102(4):1–21.

[4] W Myeong, H Myung, 2018. Development of a wall-climbing drone capable of vertical soft landing using a tilt-rotor mechanism, IEEE Access, 7:4868–4879.

[5] Z Wang, Z Zhu, H Huang, W Zhao, Y Xu, Z Zheng, N Ding, 2021. Hierarchically porous piezoresistive sensor for application to the cambered palm of climbing robot with a high payload capacity, Smart Materials and Structures, 30(7):075007.

[6] Z Wang, B He, Y Zhou, K Liu, C Zhang, 2021. Design and Implementation of a Cable Inspection Robot for Cable-Stayed Bridges. Robotica, 39(8):1417–1433.

[7] M Hernando, V Gómez, A Brunete, E Gambao, 2021. CFD Modelling and Optimization Procedure of an Adhesive System for a Modular Climbing Robot, Sensors, 21(4):1117.

[8] X Feng, L Gao, W. Tian, R Wei, Z Wang, Y Chen, 2020. Application of Wall Climbing Welding Robot in Automatic Welding of Island Spherical Tank, Journal of Coastal Research, 107(SI), 2020, 1–4.

[9] H.M. La, T.H. Dinh, N.H. Pham, Q.P. Ha, and A.Q. Pham, Automated robotic monitoring and inspection of steel structures and bridges, Robotica, 37(5), 2019, 947–967.

[10] H. Li, X. Sun, Z. Chen, L. Zhang, H. Wang, and X. Wu, Design of a wheeled wall climbing robot based on the performance of bio-inspired dry adhesive material, Robotica, 40(3), 2022, 611–624.

[11] R S Bisht, P M Pathak, S K Panigrahi, 2022. Design and development of a glass façade cleaning robot, Mechanism and Machine Theory, 168:104585.

[12] M Rostami, A H Farajollahi, 2021. Aerodynamic performance of mutual interaction tandem propellers with ducted UAV, Aerospace Science and Technology, 108:106399.

[13] O Kermorgant, 2018 A magnetic climbing robot to perform autonomous welding in the shipbuilding industry, Robotics and ComputerIntegrated Manufacturing, 53(OCT):178–186.

[14] J Hu, X Han, Y Tao, S Feng, 2022. A magnetic crawler wall-climbing robot with capacity of high payload on the convex surface, Robotics and Autonomous Systems, 148: 103907.

[15] J Liu, L Xu, S Chen, H Xu, G Cheng, J Xu, 2021. Development of a bio-inspired wall-climbing robot composed of spine wheels, adhesive belts and eddy suction cup, Robotica, 39(1):3–22.

[16] Y Liu, L Wang, S. Liu, T Mei, P Li, 2019. Design and Analysis of an Inchworm-Inspired Wall-Climbing Robot, Journal of Mechanical Transmission, 43(8):87–91.

[17] H Zhao, R Hu, P Li, A Gao, X Zhang, et al, 2020. Soft bimorph actuator with real-time multiplex motion perception, Nano Energy, 76:104926.

[18] T W Seo, Y Jeon, C Park et al, 2019. Survey on glass and façade-cleaning robots: climbing mechanisms cleaning methods and applications, International Journal of Precision Engineering and Manufacturing-Green Technology, 6(2):367–376.

[19] P Liang, X Gao, Q Zhang, et al, 2021. Design and stability analysis of a wall-climbing robot using propulsive force of propeller, Symmetry, 13(1):1–13.

Viser Technology Pte. Ltd.
Mechanical Engineering Science
DOI: 10.33142/mes.v4i1.7516

Research Article Open Access

A Novel Dual Helical Magnetorheological Fluid Micro-Robot

Zhixiang LI[1], Minglu CHI[1*], Shuaibing CHANG[2], Xiaoyan QIAN[3], Jiawen JIA[1], Jianbo LI[1], Chenyu WANG[1], Zuhua GUO[4]

1 School of Intelligent Engineering, Henan Institute of Technology, Henan Xinxiang 453000, China
2 School of Electrical Engineering and Automation, Henan Institute of Technology, Henan Xinxiang 453000, China
3 School of Economics, Henan Institute of Technology, Henan Xinxiang 453000, China
4 College of Computer Science and Technology, Henan Institute of Technology, Henan Xinxiang 453000, China

***Corresponding Author:** Minglu CHI, School of Intelligent Engineering, Henan Institute of Technology, Xinxiang, Henan, China; cmlcml86@163.com*

Abstract:
To address the problem of flexible drive control of gastrointestinal (GI) tract micro-capsule robot posture, a novel dual helix magnetorheological fluid (MRF) micro-robot (DHMRFMR) is proposed and developed in this paper. Based on the mechanical properties of magnetorheological fluid, the relationship model of magnetic field force is obtained, and the thrust model is established. Double micro DC deceleration motor is used to drive the two ends of the helical actuator to make the DHMRFMR forward and backward, by changing the external magnetic field rotation speed, direction and distance, adjust the attitude direction of the robot. Numerical simulation software ANSYS is used to analyze the motion law of external fluid of DHMRFMR, and the visualization of fluid velocity and pressure distribution is realized. The front-end helix actuator can change the flow path of the fluid, and the middle and tail of the DHMRFMR bear less pressure, which improves the stability and flexibility of the robot. The novel DHMRFMR is suitable for internal drive in bending environment, and has a good application prospect in biomedical engineering field in human intestinal unstructured environment.

***Keywords:** Dual helical actuation; Micro-robot; Magnetorheological fluid; Attitude control; Simulated analysis*

Introduction

GI tract diseases are not only prevalent in the elderly, but also in an increasing number of young people. High-risk groups need to be examined every 1-2 years, which poses severe challenges to the screening and treatment of GI tract diseases [1]. Traditional interventional gastroscopy is painful and risky, requiring patients to endure great pain. The birth of capsule endoscope greatly saves the manpower and time of GI tract disease diagnosis [2]. A capsule is swallowed with water and the whole digestive tract is traversed with gastrointestinal peristalsis without intubation. Doctors diagnose diseases on the external receiving display according to the pictures or videos taken by the capsule endoscope [3]. Compared with traditional gastroscopy, it can effectively avoid cross infection during examination in addition to eliminating the pain caused by intubation.

At present, the passive capsule robot that relies on intestinal peristalsis for GI examination has the following problems: (i) Passive capsule robots move slowly and can only move forward. (ii) The passive capsule robot is unable to stop at a problematic lesion, let alone return for a re-examination. (iii) Passive capsule robots mostly use

batteries to power their cameras. Fixed and long time shooting can produce a lot of non-diagnostic photos and waste storage space. (iv) The passive capsule robot takes a long time to check, resulting in low inspection efficiency and the possibility of missing detection [4]. Therefore, the active capsule robot came into being, can take the initiative to explore and diagnose, greatly improve the efficiency of diagnosis and treatment. The active capsule robot can reside in a suspected patient area for observation or sampling, and has various functions of active control and can interact with the doctor. In the past decade, several locomotion mechanisms were developed to provide active propulsion for capsule endoscopes, including the rotating spiral [5], inchworm-like [6], legged [7], paddle-based [8] and vibro-impact locomotion mechanisms [9].

At present, the active capsule robot is mainly divided into two ways: electric energy drive and magnetic energy drive. Tabak et al. [10] proposed a bionic

Copyright © 2022 by author(s) and Viser Technology Pte. Ltd. This is an Open Access article distributed under the terms of the Creative Commons Attribution-NonCommercial 4.0 International License (http://creativecommons.org/licenses/by-nc/4.0/), permitting all non-commercial use, distribution, and reproduction in any medium, provided the original work is properly cited.
Received on April 20, 2022; Accepted on May 10, 2022

capsule robot based on the movement principle of eukaryotic microorganisms, and controlled the capsule robot to complete multi-directional movement by a spiral tail. Tortora et al. [11-12] developed a capsule robot driven by a four-screw motor, which was applied to the diagnosis in a wide range, such as the stomach. The capsule is equipped with a visual imaging system that allows doctors to see inside the stomach using an interactive system. Norton et al. [13] proposed a wheeled micro-robot with expansion and contraction function for colon examination. Park et al. [14] developed a inchworm-like capsule to achieve forward movement through the pulling of the outrigger.

Because magnetic energy has the advantage of efficient transmission, it can not only realize wireless control, but also solve the problem of power endurance of the capsule robot. Therefore, applied magnetic field as the driving source of capsule robot has attracted extensive attention. Salerno et al. [15] proposed a "master-slave magnetic coupling" driving method for capsule robot, using a permanent magnet installed at the end of the manipulator as the main magnetic source. Through the magnetic coupling effect, the capsule robot with embedded permanent magnet will generate magnetic pull to achieve movement. Gumprecht et al. [16-17] developed a magnetic field drive device that uses electromagnets to apply magnetic force to the capsule robot to move and release drugs. Zhang et al. [18-19] studied the accuracy and feasibility of positioning and proposed a magnetic levitation system of magnetic levitation capsule robot, which controlled the steering and movement of the robot by the magnetic attraction or repulsion force generated. Qinyuan Shi et al. [20] propose an optical-magnetic fusion tracking framework to track the magnetically actuated capsule robot in real time. The proposed method utilizes the prior-known pose of external permanent magnet estimated from the optical tracking method to decouple internal permanent magnet's magnetic field from the composite magnetic field to achieve higher tracking accuracy of wireless capsule endoscopy. Puhua Tang et al. [21] designed and manufactured a set of drive systems for a capsule robot in a pipe driven by an external permanent magnet, and a measurement system of the fluid flow field in the pipe during the robot's precession.

In conclusion, regarding the operating performance of capsule robots, the existing research mainly focuses on the drive control of the capsule robot driven by electric energy or magnetic energy alone. However, the combination of electric drive and magnetic energy drive for attitude control has not been discussed. Moreover, none of the above studies considered the use of magnetorheological fluid as the magnet medium to achieve intelligent control. These unsolved issues are the motivation of our research work presented in this paper.

To overcome this problem and provide an effective attitude control method in unstructured GI tract, we have developed a novel DHMRFMR, and proposed a attitude drive control method of robot that combines electric drive and magnetic drive. The motion control of the DHMRFMR is realized by using a miniature DC reduction motor to control the front and rear helical actuator and magnetorheological fluid is used as attitude control medium. The thrust model and magnetic field force relationship model of the DHMRFMR are established, which can effectively control the attitude navigation of the robot. Finite element analysis software ANSYS is used to analyze the motion law of external fluid of DHMRFMR, and the visualization of fluid velocity and pressure distribution is realized. The results show that the front-end screw actuator can change the fluid flow path and make the middle and tail of the DHMRFMR bear less pressure. The motion stability of the DHMRFMR is improved, and it can move flexibly in the complex bending intestinal environment. This paper provides a basis for attitude control and navigation drive of micro-robot in unstructured environment.

1 Design of DHMRFMR Drive Control System

The core of the DHMRFMR drive control system is "drive" and "control" Through this system, the DHMRFMR can be controlled to move in the GI tract to achieve the purpose of stomach and intestinal examination. The overall design of DHMRFMR drive control system in this paper includes two parts: power system and pose control system. The whole control function of the DHMRFMR is shown in Figure 1.

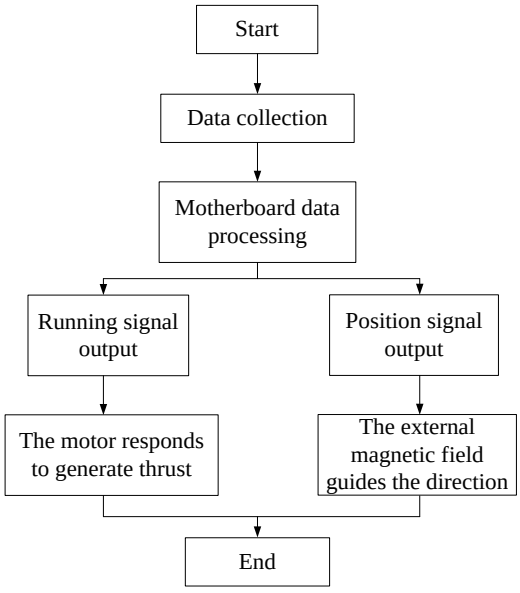

Figure 1 The whole control function of the DHMRFMR

The overall control process of the DHMRFMR is as

follows: When the DHMRFMR starts to work, a signal transmitter sends out a signal. The internal motor controller receives the signal through the signal receiver, and controls the rotation of the miniature DC reduction motor to drive the external dual helix actuator, which then generates counterthrust to push the DHMRFMR forward or backward. At the moment, the attitude control system starts the attitude adjustment function. Under the action of an external magnetic field, the magnetorheological fluid inside the DHMRFMR changes under the influence of the magnetic field, and gathers together to produce a certain force, which changes the direction of the DHMRFMR's movement. When the external magnetic field changes, the direction of action of the internal force will also change, thus changing the direction and attitude of the DHMRFMR movement.

1.1 Design of DHMRFMR Power System

Power system is mainly composed of miniature DC reduction motor, motor controller, signal receiver, signal transmitter, helix actuator and power supply, as shown in Figure 2. Due to the small size required by the medical capsule robot, there is a strict volume limitation for the power system, and the motor volume used is also small, and the performance thrust can meet the requirements. The precession device must also meet volume requirements.

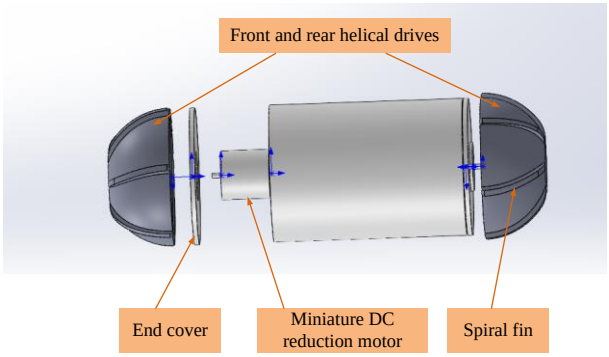

Figure 2 DHMRFMR integral structure

When the DHMRFMR enters the GI tract, the power system starts work. The external helical actuator is driven by the rotation of the motor, and the rib plate of the spiral rib will interact with the fluid in the GI tract to generate a force to push the DHMRFMR forward. The power system is driven by the front and rear dual drives, and the helical actuators at the front and rear ends of the DHMRFMR turn forward and reverse under the control of the miniature DC reduction motor. The DHMRFMR can move forward and backward without turning, which greatly improves the mobility of the robot in the GI tract.

1.2 Helical actuator Shape Design of Power System

The semicircular shape of the helical actuator can reduce the scratches on the GI tract wall during the rotation of the spiral ribs of the DHMRFMR, and reduce the resistance of the robot when moving in the liquid environment. The helical actuator is 3D printed with medical materials, which has the characteristics of corrosion resistance, good wear resistance and stable performance. The helical actuator is light in weight and stable in structure. The DHMRFMR helical actuator is shown in Figure 3.

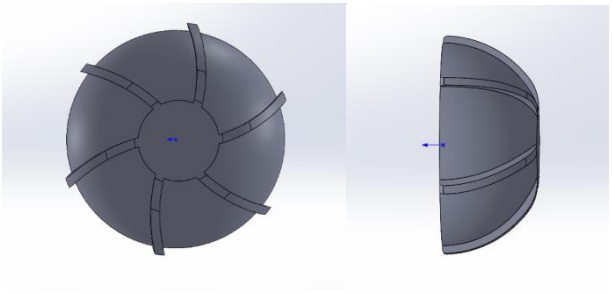

Figure 3 Helical drive for DHMRFMR

1.3 Miniature DC Reduction Motor for Dual Helix Power System

The DHMRFMR drive control power system uses two DC reduction motors to drive the front and rear helical actuators. The motor is easy to control, good stability, strong adaptability to the environment. The experiment is carried out in a transparent plexiglas tube, so the open-loop control method can meet the demand of speed control. The motor has a voltage range of 0.2-6 V, rated voltage of 3 V, maximum speed of 1200 r/min, current of 25 mA, and power of 0.1 W. The total length of motor is 16.5 mm, the diameter of reduction box is 6 mm, and the reduction ratio of reduction box is 1:26, as shown in Figure 4.

Figure 4 Miniature DC reduction motor

The power system adopts wireless remote control, which is composed of radio frequency transmitter and radio receiver. Wireless transmission adopts the point control mode. Press the button to turn forward, and press

the button again to reverse the motor, as shown in Figure 5. The wireless transmitter has small volume, low power consumption and wide voltage range. In standby state, the current is only 0.05 mA, and the working voltage is DC 3V. It has low energy consumption and can work for a long time.

The size of the wireless receiver is 21mm×11mm×5mm, the voltage range is DC 3V-12V, and the maximum current is 0.4 A. The receiver itself has overcurrent protection function. The black line is the negative pole of the power supply, the red line is the positive pole of the power supply, and the yellow line is the receiver's two outputs, controlling two DC reduction motors. The power supply is lithium battery with a size of 19mm×10mm×4mm and a voltage of 3.7 V, as shown in Figure 6.

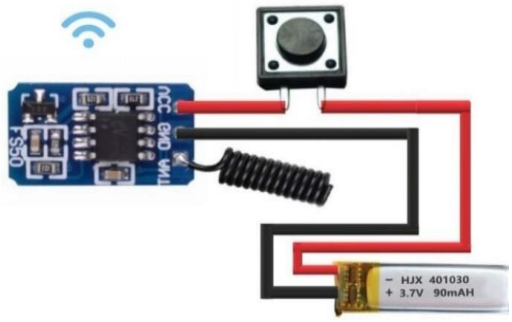

Figure 5 Wireless control transmitter

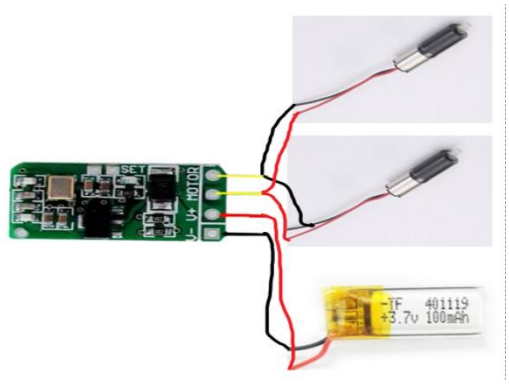

Figure 6 Wireless receiver

1.4 Analysis and Calculation of Helical Thrust Force of Power System

Microrobots move forward in a closed environment by pushing the fluid at the front with the helical head. The fluid will be obstructed in the reverse direction, and the fluid will enter the rear area along the side of the DHMRFMR. If the swimming speed of the DHMRFMR is high, the fluid on the surface is laminar flow, and the fluid stuck to the surface of the robot rotates synchronously with the robot. If the fluid does not pass quickly through the side of the DHMRFMR to the rear area, turbulent conditions can occur. The condition for satisfying Bernoulli's equation is that the fluid is in laminar flow state, which is the ideal state.

As the DHMRFMR spins forward, the fluid in front of it is separated by the robot and flows sideways. The DHMRFMR is subjected to axial fluid resistance, called frictional resistance Ff. The fluid has a certain viscosity, the part of the fluid near the DHMRFMR surface will speed up, forming a boundary layer on the surface. At this point, the fluid pressure on the front and back ends of the DHMRFMR is different, forming fluid resistance, known as differential pressure resistance Fc. The total resistance of the DHMRFMR is the sum of Ff and Fc, that is:

$$F_{to} = F_f + F_c \tag{1}$$

Frictional resistance and differential pressure resistance can be obtained by multiplying the kinetic energy of the flow per unit volume by a certain area, and then multiplying by the drag coefficient, can be expressed as

$$F_f = C_f \frac{\rho v^2}{2} S_f \tag{2}$$

$$F_c = C_p \frac{\rho v^2}{2} S_p \tag{3}$$

where *Cf* and *Cp* are the drag coefficients of friction resistance and differential pressure resistance respectively, *Sf* is the area under shear stress, *Sp* is the projected area of the object perpendicular to the direction of flow velocity, ρ is density, and v is the speed of the DHMRFMR. Therefore, the total resistance can be expressed as

$$F_{to} = C_D \frac{\rho v^2}{2} S \tag{4}$$

where *CD* is the total drag coefficient, S is the area projected against flow of the object in the vertical direction of flow velocity, so S=*Sp*. When the total driving force of the DHMRFMR is equal to the total fluid resistance, the total thrust of the DHMRFMR can be obtained.

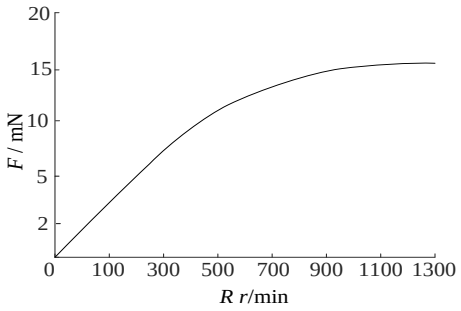

Figure 7 Diagram of helical thrust force changes with rotational speed

As shown in Figure 7, the helical thrust changes with the speed. With the increase of the speed of the miniature DC reducer motor of the power system, the helical thrust of the power system gradually increases. When the speed reaches 1000 r/min, the thrust is kept at about 15 mN, and the speed continues to increase, and the

thrust is kept constant, indicating that the system has reached a dynamic equilibrium state at this time.

2 Pose Control System for DHMRFMR

The pose control system is used to adjust the pose direction of the DHMRFMR. Because the GI tract is an unstructured meandering environment, DHMRFMR needs to be able to change direction continuously during movement. DHMRFMR pose control is realized by coupling control of external magnetic field and internal magnet.

2.1 Fluid Mechanics Properties of MF

MF is a kind of intelligent fluid. The rheological properties of MF will change when there is a certain intensity of magnetic field in the environment, and it will change from a fluid to a solid with a certain viscoelasticity. If the magnetic field disappears, it will return from a solid with a certain viscoelasticity to the original liquid.

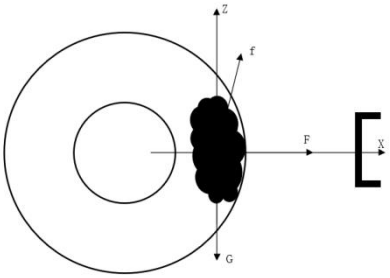

Figure 8 Force analysis of MF

According to this characteristic, the yield stress of the fluid can be controlled by changing the magnetic field intensity of the surrounding environment, so as to realize intelligent control of the magnetorheological fluid. The force on MF is shown in Figure 8. When the MF is in a certain magnetic field, the magnetic force is

$$F = \mu_0 V(M \cdot \nabla)H = V(M \cdot \nabla)B \tag{5}$$

where F is magnetic field force, $\mu 0$ is vacuum permeability, V is volume of MF, M is magnetization, ∇ is magnetic field gradient operator, H is magnetic field intensity, B is magnetic induction intensity. The magnetic induction intensity B and magnetization intensity M can be decomposed along X, Y and Z axes, which are Bx, By, Bz and Mx, My and Mz, respectively.

$$\begin{bmatrix} F_x \\ F_y \\ F_z \end{bmatrix} = V \begin{bmatrix} M_x \frac{\partial B_x}{\partial_x} + M_y \frac{\partial B_x}{\partial_y} + M_z \frac{\partial B_x}{\partial_z} \\ M_x \frac{\partial B_y}{\partial_x} + M_y \frac{\partial B_y}{\partial_y} + M_z \frac{\partial B_y}{\partial_z} \\ M_x \frac{\partial B_z}{\partial_x} + M_y \frac{\partial B_z}{\partial_y} + M_z \frac{\partial B_z}{\partial_z} \end{bmatrix} \tag{6}$$

2.2 Control Principle of Pose Control System

The pose control system mainly uses magnetic field environment composed of MF and external magnets to control the pose direction of the DHMRFMR. The shell of the DHMRFMR is a hollow cavity inside, which is used to contain MFs. When the DHMRFMR is placed in the magnetic field generated by the external magnetic field, the MF in the cavity is magnetized by the external magnetic field, which turns the originally uniformly distributed liquid into a concentrated spiky-shaped solid. The MF, which is concentrated together, creates a magnetic force under the action of a magnetic field, which changes the direction of motion of the DHMRFMR. By changing the distance and position between the external magnetic field and the internal MF, the position and attitude of the DHMRFMR can be changed.

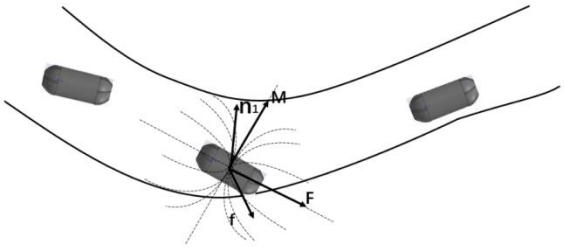

Figure 9 Attitude control diagram

Figure 9 is the attitude control diagram of the DHMRFMR. The dotted line represents the external magnetic field around the DHMRFMR. In Figure 8, the area with dense dotted line distribution indicates that the magnetic field intensity of the region is strong, while the area with sparse dotted line distribution indicates that the magnetic field intensity is weak. When the DHMRFMR is in the area with dense magnetic field lines, the MF inside the robot will be pushed and pulled more, and the direction of motion will change more easily.

3 Simulation Test Analysis of DHMRFMR System

To verify the correctness of the theoretical analysis and the feasibility of the device, the control system of DHMRFMR is developed. ANSYS 2021R1 software is used to simulate the velocity and pressure distribution of the DHMRFMR to realize the visualization of the flow field. Firstly, the model of driving motor and precession device is built by simulation software, and then the motor and precession device of the driving system are assembled and debugged, as shown in Figure 10. And finally the simulation is carried out by ANSYS software.

Figure 10 Attitude control diagram

The thrust, attitude and guidance of the DHMRFMR power device are tested, the value of thrust and the thrust adjustment of the power system under different working conditions are calculated by analyzing the simulated data, and the stability of the DHMRFMR under different thrust is analyzed. The structural parameters of the DHMRFMR are shown in Table 1.

Tab 1 Structural parameters of the DHMRFMR

Parameters	Notation	DHMRFMR
Length /(mm)	L	75
Diameter /(mm)	D	26
Mass /(g)	G	48.1
Helical actuator diameter (Maximum) /(mm)	Ds	27
Height of spiral ribs /(mm)	ka	1.2
Width of spiral groove (Maximum) /(mm)	N1	16
Width of spiral ribs /(mm)	N2	1.5
Helix angle /(°)	β	20
Working speed /(r/min)	n	1000

Before the simulation analysis, it is necessary to conduct 3D modeling of the DHMRFMR in Solidworks and 3D printing and manufacturing according to the 3D model. The 3D model and physical prototype are shown in Figure 11 (a) and Figure 11 (b), respectively.

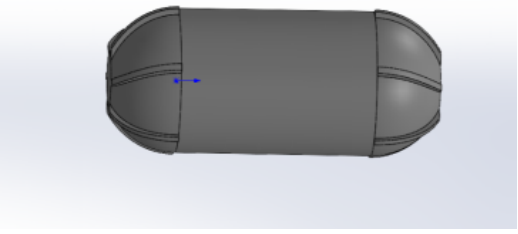

(a) 3D model of DHMRFMR

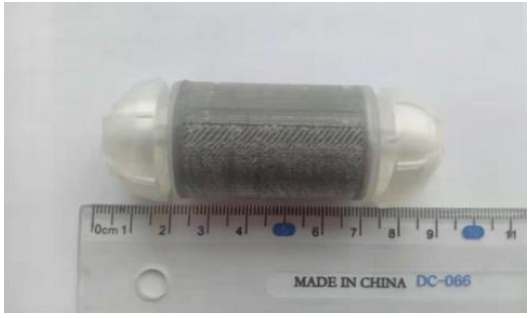

(b) Prototype of a DHMRFMR

Figure 11 Solidworks 3D model and prototype of DHMRFMR

The continuity equation and Navier-Stokes equation are regarded as the governing equations.

The continuity equation can be written as:

$$\frac{\partial(\rho u)}{\partial x}+\frac{\partial(\rho v)}{\partial y}+\frac{\partial(\rho w)}{\partial z}=0 \tag{7}$$

The Navier-Stokes equation can be expressed as:

$$\begin{cases}\dfrac{\partial(\rho u)}{\partial t}+div(\rho uU)=div(\mu gradu)-\dfrac{\partial p}{\partial x}+F_x\\ \dfrac{\partial(\rho v)}{\partial t}+div(\rho vU)=div(\mu gradv)-\dfrac{\partial p}{\partial y}+F_y\\ \dfrac{\partial(\rho w)}{\partial t}+div(\rho wU)=div(\mu gradw)-\dfrac{\partial p}{\partial z}+F_z\end{cases} \tag{8}$$

where u, v and w are the components of fluid velocity U on each coordinate axis, ρ and μ are the density and dynamic viscosity of fluid respectively, p is pressure, Fx, Fy and Fz are the mass force of fluid element on each coordinate axis.

The fluid in the pipeline is meshed and the DHMRFMR surface meshes are locally encrypted to improve the calculation accuracy. The fluid type is set as liquid, the dynamic viscosity is 1.0 Pa s, and the rotation axis of the DHMRFMR model is set as along the Y-axis. Establish the cloud picture of the operation interface, select the unit and data displayed on the operation interface, and start the simulation operation after checking the correctness.

When the DHMRFMR runs at a certain speed in the fluid, the velocity distribution cloud of the surrounding environment is shown in Figure 12. In the Figure, the external fluid moves with the DHMRFMR at the same time and has a follow-up effect. The farther away from the DHMRFMR, the lower the degree of fluid flow. At the far end, the fluid flow velocity is close to 0. This results in the fluid velocity on the surface being roughly the same as the DHMRFMR velocity. At the same time, it can be seen that the fluid velocity at the back end of the DHMRFMR is higher and has a greater driving force.

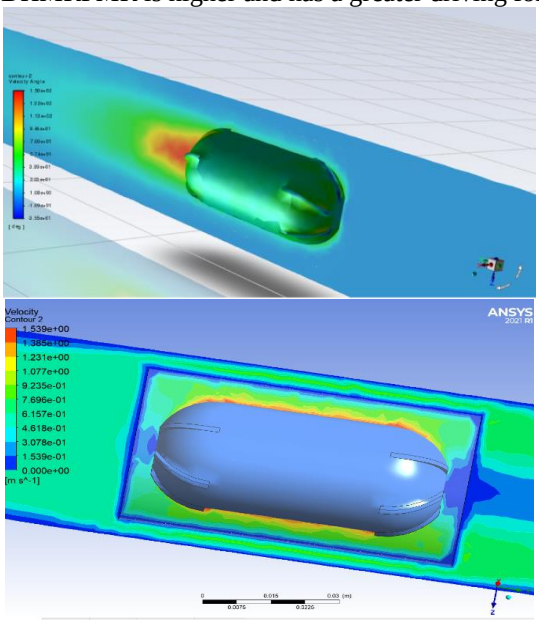

Figure 12 Cloud image of motion speed of DHMRFMR model

When the DHMRFMR runs, the ambient pressure of the liquid will change, and the helical actuator of the DHMRFMR model will also be subjected to a certain amount of fluid push back pressure. The pressure distribution cloud diagram generated by the operation is shown in Figure 13. In the Figure, the front-end of the DHMRFMR is subjected to a large fluid impact pressure, up to 274 Pa.

Because the pressure of the front-end helical actuator is larger, the fluid flow path is changed, and the middle and tail of the DHMRFMR bear less pressure, which improves the stability and flexibility of the DHMRFMR.

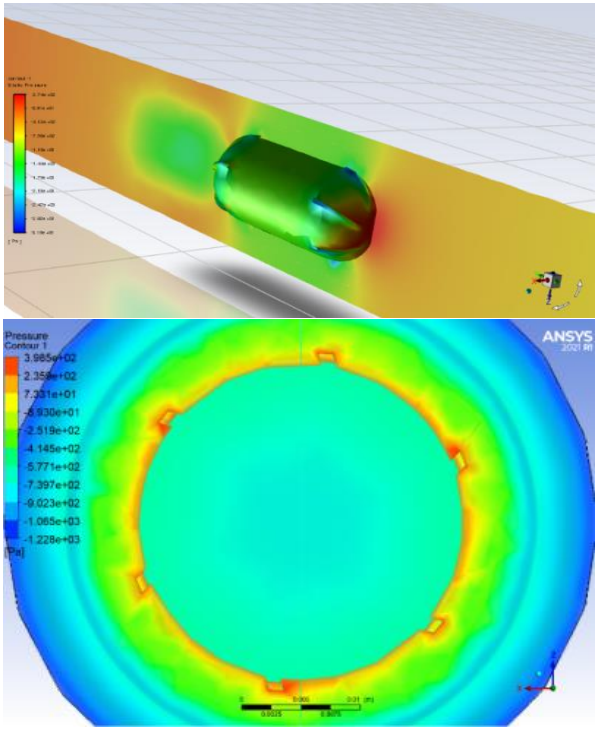

Figure 13 Pressure cloud diagram of DHMRFMR model

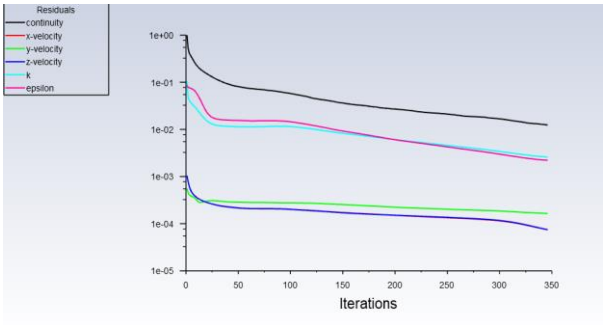

Figure 14 Floating point variation of simulation results

The simulation results show that the floating point variation of the DHMRFMR model is relatively stable. Floating point numbers do not generate large fluctuations, and there is no floating point overflow during operation. Floating point numbers form a relatively smooth curve, as shown in Figure 14. The operation results verify that the designed system is relatively stable and meets the design requirements.

4 Conclusions

In this paper, theoretical modeling and finite element simulation are carried out for important problems in attitude control of GI tract DHMRFMR. The simulation results are in good agreement with theoretical analysis. The main conclusions are as follows:

(1) A novel DHMRFMR is designed and developed, which consists of a miniature DC reduction motor, a motor controller, a signal receiver, a signal transmitter, a helical actuator, a MF cavity and a power supply. The DHMRFMR can move forward and backward without turning, with good movement flexibility.

(2) The DHMRFMR drive control system consists of pose control system and power system. The magnetic field force relationship model of MF is obtained and the thrust model is established. The pose control of DHMRFMR is realized by coupling control of external magnetic field and internal magnet. By changing the distance and position between the external magnetic field and the internal MF, the position and attitude direction of the DHMRFMR in the process of motion can be realized.

(3) Finite element analysis software ANSYS is utilized to analyze the external fluid movement law of DHMRFMR, and the visualization of fluid velocity and pressure distribution is realized. When the DHMRFMR moves in a fluid at a certain speed, the surrounding fluid moves simultaneously. Further away from the DHMRFMR, the flow velocity of the fluid is almost stationary. The front-end helical actuator can change the flow path of the fluid and improve the stability and flexibility of the DHMRFMR.

The breakthrough in the driving and control technology of the novel DHMRFMR has laid a clinical foundation for diagnosis and treatment and targeted drug delivery in the unstructured environment of human GI tract, and has a good application prospect.

Conflict of Interest

Te author declare that there is no conflict of interest regarding the publication of this paper.

Acknowledgement

This work was supported by the Key Research Development and Promotion Special Project of Henan Province, under Grant 212102310119 and 212102210358, Scientific Research Foundation for High-level Talents of Henan Institute of Technology, under Grant KQ1869, Research and Practice Project of Higher Education Teaching Reform in Henan Province, under Grant 2021SJGLX289, University-Industry Collaborative Education Program, under Grant 202101187010 and

202102120046, Innovation and Entrepreneurship Training Program for College Students of Henan Province, under Grant 202211329011, Educational and Teaching Reform Research and Practice Project of Henan Institute of Technology, under Grant 2021-YB023 and JJXY-2021005, Innovative Education Curriculum Construction Project of Henan Institute of Technology, under Grant CX-2021-005, 2022 Xinxiang Federation of Social Sciences Research topic, under Grant SKL-2022-254 and SKL-2022-228, 2022 Annual Research Topic of Henan Federation of Social Sciences, under Grant SKL-2022-2692.

References

[1] Bray F, Ferlay J, Soerjomataram I, et al, 2018. Global cancer statistics 2018: GLOBOCAN estimates of incidence and mortality worldwide for 36 cancers in 185 countries. CA: a cancer journal for clinicians, 68(6): 394-424.

[2] Rondonotti E, Spada C, Adler S, et al, 2018. Small-bowel capsule endoscopy and device-assisted enteroscopy for diagnosis and treatment of small-bowel disorders: European Society of Gastrointestinal Endoscopy (ESGE) Technical Review. Endoscopy, 50(4): 423-446.

[3] Bouchard S, Ibrahim M, Van Gossum A, 2014. Video capsule endoscopy: perspectives of a revolutionary technique. World Journal of Gastroenterology: WJG, 20(46): 17330.

[4] Slawinski P R, Obstein K L, Valdastri P, 2015. Capsule endoscopy of the future: What's on the horizon. World journal of gastroenterology: WJG, 21(37): 10528.

[5] Sendoh M, Ishiyama K, Arai K I, 2003. Fabrication of magnetic actuator for use in a capsule endoscope. IEEE Transactions on Magnetics, 39(5): 3232-3234.

[6] Kim B, Park S, Park J O, 2009. Microrobots for a capsule endoscope. IEEE/ASME International Conference on Advanced Intelligent Mechatronics. IEEE: 729-734.

[7] Quirini M, Menciassi A, Scapellato S, et al, 2008. Design and fabrication of a motor legged capsule for the active exploration of the gastrointestinal tract. IEEE/ASME transactions on mechatronics, 13(2): 169-179.

[8] Park H, Park S, Yoon E, et al, 2007. Paddling based microrobot for capsule endoscopes. Proceedings 2007 IEEE International Conference on Robotics and Automation. IEEE, : 3377-3382.

[9] Liu Y, Wiercigroch M, Pavlovskaia E, et al, 2013. Modelling of a vibro-impact capsule system. International Journal of Mechanical Sciences, 66: 2-11.

[10] Tabak A F, Yesilyurt S, 2012. Experiments on in-channel swimming of an untethered biomimetic robot with different helical tails. 4th IEEE RAS & EMBS International Conference on Biomedical Robotics and Biomechatronics (BioRob). IEEE: 556-561.

[11] De Falco I., Tortora G, Dario P., et al, 2014. An integrated system for wireless capsule endoscopy in a liquid-distended stomach. IEEE Transactions on Biomedical Engineering, 61(3):794-804.

[12] Tortora G., Valdastri P., Susilo E., et al, 2009. Propeller-based wireless device for active capsular endoscopy in the gastric district. Minimally Invasive Therapy & Allied Technologies, 18(5):280-290.

[13] Norton J, Hood A, Neville A, et al, 2016. RollerBall: a mobile robot for intraluminal locomotion. 6th IEEE International Conference on Biomedical Robotics and Biomechatronics (BioRob). IEEE: 254-259.

[14] Park H J, Kim D, Kim B, 2012. A robotic colonoscope with long stroke and reliable leg clamping. International Journal of Precision Engineering & Manufacturing, 13(8):1461-1466.

[15] Salerno M, Rizzo R, Sinibaldi E, et al, 2013. Force calculation for localized magnetic driven capsule endoscopes. IEEE International Conference on Robotics and Automation. IEEE: 5354-5359.

[16] Gumprecht J D J, Lueth T C, Khamesee M B, 2013. Navigation of a robotic capsule endoscope with a novel ultrasound tracking system. Microsystem technologies, 19(9): 1415-1423.

[17] Hosseini S., Mehrtash M, Khamesee M, 2011. Design, fabrication and control of a magnetic capsule-robot for the human esophagus. Microsystem Technologies, 17(5-7): 1145-1152.

[18] Zhang X, Mehrtash M, Khamesee M, 2016. Dual-axial motion control of a magnetic levitation system using hall-effect sensors. IEEE/ASME Transactions on Mechatronics, 21(2): 1129-1139.

[19] Mehrtash M, Khamesee M, Tsuda N., et al, 2012. Motion control of a magnetically levitated microrobot using magnetic flux measurement. Microsystem Technologies, 18(9-10): 1417-1424.

[20] Shi Q, Liu T, Song S, et al, 2021. An optically aided magnetic tracking approach for magnetically actuated capsule robot. IEEE Transactions on Instrumentation and Measurement, 70: 1-9.

[21] Tang P, Liang L, Guo Z, et al, 2021. Orthogonal optimal design of multiple parameters of a magnetically controlled capsule robot. Micromachines, 12(7): 802.

Publisher: Viser Technology Pte. Ltd.

URL: www.viserdata.com

Add.:21 Woodlands Close, #08-18,

Primz Bizhub SINGAPORE (737854)